HIGHLY-DOPED SILICON BASED PHOTONIC DEVICES FOR MID-INFRARED LIGHT ABSORPTION

A THESIS SUBMITTED TO

THE GRADUATE SCHOOL OF ENGINEERING AND SCIENCE

OF BILKENT UNIVERSITY

IN PARTIAL FULFILLMENT OF THE REQUIREMENTS FOR

THE DEGREE OF

MASTER OF SCIENCE

IN

ELECTRICAL AND ELECTRONICS ENGINEERING

By

Kazim Görgülü

July 2017

HIGHLY-DOPED SILICON BASED PHOTONIC DEVICES FOR MID-INFRARED LIGHT ABSORPTION
By Kazim Görgülü
July 2017

We certify that we have read this thesis and that in our opinion it is fully adequate, in scope and in quality, as a thesis for the degree of Master of Science.

Ekmel Özbay(Advisor)

Bayram Bütün(Co-Advisor)

Ayhan Altıntaş

Sefer Bora Lişesivdin

Approved for the Graduate School of Engineering and Science:

Ezhan Karaşan
Director of the Graduate School

ABSTRACT

HIGHLY-DOPED SILICON BASED PHOTONIC DEVICES FOR MID-INFRARED LIGHT ABSORPTION

Kazim Görgülü
M.S. in Electrical and Electronics Engineering
Advisor: Ekmel Özbay, Co-Advisor: Bayram Bütün
July 2017

Electromagnetic wave absorbers have the potential to enable important applications in the mid-infrared wavelength range such as thermal imaging and infrared spectroscopy. The choice of absorbing material has significant implications for the ultimate utility of any photonic device or structure. So far, traditional metals are employed as common absorbing materials, especially in metamaterial designs. However, many of these metals react with the atmosphere or water, limiting their utility for a wide range of applications. There are many materials, other than conventional metallic components, that exhibit lossy properties and provide advantages in device performance, design exibility, fabrication, integration, and tunability. Here, we investigate highly doped silicon as an efficient absorbing material for the mid-infrared regime. The absorption is achieved by the free carriers in the silicon which can be spectrally tuned by controlling its carrier concentration.

Most of the resonant absorbers suffer from narrow operating absorption waveband. A common approach is to use multiple resonance centers to increase bandwidth. However, the number of resonators combined within the same unit cell is limited. We propose highly doped silicon based absorbers with a patterned silicon-on-insulator substrate that provide enhanced bandwidth without compromising absorption performance. Broadband absorption is achieved by the combined effects of bulk absorption, and vibrational and plasmonic absorption resonances. Moreover, we investigate black silicon concept for mid-infrared regime. The structures investigated unveil wideband and efficient absorbers. An analytical description of the wave propagation in black silicon texture is presented, showing agreement with the experiment and the computational analysis.

Some other applications, such as selective thermal emitters and detectors, and

bio-chemical and refractive index sensors, require narrow absorption bands. Plasmonic absorbers typically have narrow resonance bands and they can be utilized in highly sensitive detection schemes. Traditional metals are common materials for these applications. However, apart from their fabrication challenges, they have extremely large, negative permittivity. This feature of metals significantly limits their plasmonic mode confinement in the mid-infrared regime. In this regime, highly doped silicon is a promising plasmonic material for sensing applications owing to its suitable plasma frequency. Here, we demonstrate plasmonic perfect absorbers based on high conductivity silicon and investigate refractive index sensing performance of the absorbers.

Keywords: silicon, mid-infrared, absorber, plasmonics, black silicon, refractive index sensing.

ÖZET

YÜKSEK DERECEDE DOPLANMIŞ SİLİKON TABANLI FOTONİK YAPILAR İLE ORTA-KIZILÖTESİ IŞIĞIN EMİLİMİ

Kazim Görgülü
Elektrik ve Elektronik Mühendisliği, Yüksek Lisans
Tez Danışmanı: Ekmel Özbay, Eş Danışman: Bayram Bütün
Temmuz 2017

Elektromanyetik dalga soğurucuları orta-kızılötesi bölgede termal görüntüleme ve kızılötesi spektroskopi gibi önemli uygulamalara imkan sağlamaktadırlar. Soğurucu materyalin seçimi herhangi bir fotonik yapının kullanışlılığında çok önemli bir etkiye sahiptir. Bu zamana kadar, özellikle de metamalzemeli yapılarda, geleneksel metaller soğurucu materyal olarak kullanılmışlardır. Fakat, bu metallerin bir çoğu atmosferle veya su ile tepkimeye girmekte ve bu da onların birçok uygulamada kullanımını sınırlandırmaktadır. Bu metallerin dışında soğurucu özelliklere sahip birçok materyal bulunmakta ve bu materyaller performans, tasarım esnekliği, üretim, entegrasyon ve tonlanabilirlik açısından avantaj sağlamaktadır. Biz burada, yüksek düzeyde doplanmış silikonu orta-kızılötesi bölgede soğurucu bir materyal olarak inceledik. Soğurma, silikon içerisindeki serbest taşıyıcılar ile sağlanmakta ve silikonun içerisindeki taşıyıcı yoğunluğu değiştirilerek kontrol edilebilmektedir.

Rezonant soğurucuların çoğu dar işletim dalgabandına sahiptir. Çoklu rezonans merkezlerinin aynı anda kullanılması band genişliğini artırmanın yaygın yöntemidir. Ancak, aynı birim yapıdaki rezonatör sayısı sınırlıdır. Biz burada soğurma veriminden taviz vermeden yüksek derecede doplanmış silikon tabanlı, şekillendirilmiş yalıtkan üzerinde silikon alttaş kullanarak, ultra geniş bantlı bir soğurucu önerdik. Geniş bantlı soğurma özelliği kütle (bulk) soğurma, vibrasyonel ve plazmonik soğurmanın birleşiminden gelmektedir. Biz ayrıca bu çalışmaya ek olarak siyah silikon kavramını orta-kızılötesi ışık için inceledik. Bu yapılar ile de geniş bantlı ve yüksek performanslı soğurucular elde ettik. Elektromanyetik dalganın bu yapı ile etkileşimini analitik olarak açıkladık ve deneysel ve simulasyon sonuçları ile karşılaştırdık.

Biyo-kimyasal ve kırılma endeksi sensörleri ile seçici termal yayıcılar ve dedektörler gibi bazı uygulamalar ise dar bir soğurma bandı gerektirirler. Plazmonik soğurucular genelde dar soğurma bandına sahiptirler ve bu yüzden yüksek derecede hassas algılama düzeneklerinde kullanılabilirler. Bu uygulamalarda geleneksel metaller yaygın olarak kullanılırlar. Fakat, üretimdeki zorluklarının yanında metaller orta-kızılötesi bölgede çok negatif bir elektriksel geçirgenliğe sahiptir bu yüzden metallerin plazmonik mod toplanması zorlaşmaktadır. Bu bölgede yüksek derecede doplanmış silikon, uygun plazma frekansından dolayı, gelecek vaad eden bir materyaldir. Biz burada yüksek derecede doplanmış silikon kullanarak yüksek verimlilikte bir plazmonik soğurucu tasarladık ve bu soğurucuyu kırılma endeksi sensörü olarak inceledik.

Anahtar sözcükler: silisyum, orta-kızılötesi, soğurucu, plazmonik, siyah silisyum, kırılma endeks sensörü.

Acknowledgement

I would like to thank my former advisor Prof. Ali K. Okyay for his guidance in the first year of my master's degree studies. I also thank my current advisor and co-advisor Prof. Ekmel Özbay and Dr. Bayram Bütün for their guidance in the second year of my master's degree studies.

I would like to thank Prof. Ayhan Altıntaş and Prof. S. Bora Lişesivdin for being members of my thesis committee and their valuable comments.

I am grateful to Dr. Mehmet Yılmaz and Dr. Kağan Topallı for their help and support. I would like to thank Abdullah Gök for his help and guidance in my studies. I thank Sami Bolat for his devoted help in my lab works. I also thank Zülkarneyn and Sina for their help and for being nice friends to me.

I acknowledge TUBITAK BIDEB for providing me a M.Sc. scholarship.

Contents

List of Figures

Chapter 1

Introduction

1.1 Background and Motivation

Electromagnetic (EM) wave absorbers absorbs incident radiation at the frequency of operation by suppressing reflection, transmission and scattering in the structure. EM wave absorbers are of great importance due to their potential in various applications. These applications briefly include: emitters, sensors, anti-reflective coatings, spatial light modulators, photovoltaics etc.

Considerable recent research has focused on increasing the efficiency of energy absorption processes. Highly efficient light absorption with structures consist of single layer or multiple layers of lossy materials [1–3]. Metamaterial absorbers are also widely explored as promising candidates to enhance EM wave absorption at microwave, terahertz, infrared, and visible frequencies [4–8]. However, confined by resonance nature of the unit structures, these metamaterial absorbers generally absorb light within a narrow wavelength range. Researchers tried to increase the absorption waveband by exploiting multiple resonances simultaneously, for applications where broadband absorption is desirable.

Some applications, such as selective thermal emitters and detectors, and biochemical and refractive index sensors, require narrow absorption bands [9, 10]. Plasmonic absorbers typically have narrow resonance bands and therefore they can be utilized in spectrally selective detection schemes such as uncooled microbolometers [4]. Narrow resonance bands are highly desirable in sensing applications in order to detect minute changes in the environment. Plasmonic resonances, confined to a metal dielectric surface, are extremely sensitive to the refractive index of the surrounding dielectric medium. Such strong dependency on the refractive index of the surrounding dielectric medium paves the way for ultra-sensitive label-free refractive index sensing applications [11, 12].

All examples mentioned above utilize conventional metallic components, such as gold and silver, as their material building blocks. In commonly used metals, the magnitude of the real part of the permittivity is very large at mid-infrared wavelengths. This feature of metals significantly limits their plasmonic mode confinement in the mid-infrared regime [13]. Moreover, the devices made of conventional metals are not compatible with CMOS processes (such as Au) and that have degradation problem upon exposure to air and humidity such as Ag. Alternatively, there are many materials, other than conventional metals, that provide advantages in device performance, integration, and tunability such as semiconductors, transparent conducting oxides, metal nitrides, perovskite oxides, silicides, germanides, and 2D materials [13, 14]. Among these materials, semiconductors have attracted great interest due to their well-established fabrication and integration technology. To date, various plasmonic and metamaterial absorbers have been studied with different semiconductors including ZnO, InAs, InSb, Ge [13,15,16]. Demonstration of plasmonic effects by silicon in the infrared region is carried out by others [17,18]. Excitation of plasmonic resonances on silicon surface is very important for CMOS compatible devices in the infrared region. In addition to silicon plasmonics, needle-like black silicon structures emerged as interesting material with broadband absorbance of more than 99%. So far black silicon structures are presented in the visible and the near-infrared region mostly for photovoltaic and surface enhanced sensing applications. Doping of silicon can bring black silicon concept to the mid-infrared range.

In this thesis, we investigate highly-doped silicon as a material for obtaining highly efficient and ultra-wideband absorbers operating in the mid-infrared region. We also study the refractive index sensing performance of highly-doped silicon based perfect absorbers.

1.2 Thesis Overview

In this first chapter, we introduce conventional absorbers. We emphasize plasmonic and metamaterial absorbers made by conventional metals. Then, we discuss about alternative absorber materials and their advantages over conventional metals and we present highly doped silicon as a material for absorber in the mid-infrared range.

In Chapter 2, we present theoretical background and methods. Plasmonic absorption is one of the main absorption mechanism for the proposed structures in this thesis. Therefore, we investigate surface plasmon polaritons at a single interface and multilayer systems. Numerical calculations based on finite difference time domain method are also frequently used. Therefore, we describe the simulation method. Then we give Drude model and extraction of optical constants of highly doped silicon via ellipsometric measurements in this chapter.

In chapter 3, we give detailed background on the previous works related with wideband absorbers operating in the mid-infrared regime. We present design and fabrication of the structure. Then, we provide simulation and experimental results, and discuss about absorption mechanisms. Then, we talk about the dependence of the absorption spectrum on the doping density of silicon and angular dependence of the absorption spectrum.

In Chapter 4, a detailed background on the previous works related with plasmonic perfect absorbers used for refractive index sensing is given. Then, usage of silicon for refractive index sensing operating in the mid-infrared range is emphasized. Design and fabrication of the structure is discussed. Simulation and experimental results for the perfect absorbers with different periodicity for normal and oblique incidences is presented. Then refractive index sensing experiment is provided. Finally, the dependence of sensing performance of the structure on the doping concentration of silicon is discussed.

Chapter 5 is about moving the black silicon concept from visible to the infrared region. A detailed background on the previous works related with black silicon concept is given. Then fabrication of black silicon pattern and implementing this pattern in the simulation environment is described. Then, an analytical description of the wave propagation in black silicon texture is given. Comparison of the experimental, simulated and analytical reflection results is presented.

Chapter 6 summarizes our findings and provides the future research directions.

Chapter 2

Theory and methods

2.1 Surface plasmons

2.1.1 Wave Equation

We will start by reviewing Maxwell's equations. The relation between four macroscopic fields $\vec{D}$ (the dielectric displacement or electric flux density), $\vec{E}$ (the electric field), $\vec{H}$ (the magnetic field), and $\vec{B}$ (the magnetic induction or magnetic flux density) in differential form is:

$$\nabla \cdot \vec{D} = \rho_{ext} \tag{2.1}$$

$$\nabla \cdot \vec{B} = 0 \tag{2.2}$$

$$\nabla \times \vec{E} = -\frac{\mu_0 \partial \vec{H}}{\partial t} \tag{2.3}$$

$$\nabla \times \vec{H} = \vec{J}_{ext} + \frac{\partial \vec{D}}{\partial t} \tag{2.4}$$

The flux density vectors can also be expressed as:

$$\vec{D} = \varepsilon_0 \vec{E} + \vec{P} \tag{2.5}$$

$$\vec{B} = \mu_0 \vec{H} + \mu_0 \vec{M} \tag{2.6}$$

where ε_0 and μ_0 are the permittivity and permeability of vacuum, respectively. $\vec{P}$ is polarization density and $\vec{M}$ is magnetization density. We will only deal with nonmagnetic media, we do not need to consider magnetization. In a linear, isotropic and homogeneous medium electric polarization can be expressed as:

$$\vec{P} = \varepsilon_0 \chi \vec{E} \tag{2.7}$$

Then flux density vectors become:

$$\vec{D} = \varepsilon_0 \varepsilon \vec{E} \tag{2.8}$$

$$\vec{B} = \mu_0 \mu \vec{H} \tag{2.9}$$

where $\varepsilon = 1 + \chi$ is the dielectric constant or relative permittivity and $\mu = 1$ relative permeability of the nonmagnetic medium.

The wave equation can be obtained for a source free medium by first applying a curl on eq. 2.3 and substituting eq 2.4 into 2.3.

$$\nabla \times \nabla \times \vec{E} = -\frac{\mu_0 \partial^2 \vec{D}}{\partial t^2} \tag{2.10}$$

Using the vector identity, $\nabla \times \nabla \times \vec{E} \equiv \nabla(\nabla \cdot \vec{E}) - \nabla^2 \vec{E}$ and due to source free medium $\nabla \cdot \vec{D} = 0$ wave equation becomes:

$$\nabla^2 \vec{E} - \frac{\mu_0 \varepsilon_0 \varepsilon \partial^2 \vec{E}}{\partial t^2} = 0 \tag{2.11}$$

Assuming harmonic time dependence, $E(\vec{r}, t) = E(r)e^{-j\omega t}$ equation 2.11 becomes:

$$\nabla^2\vec{E} + {k_0}^2\varepsilon\vec{E} = 0 \tag{2.12}$$

where $k_0 = \omega\sqrt{\mu_0\varepsilon_0} = \frac{\omega}{c}$ is the wave vector of the wave in free space.

For harmonic time dependence we arrive following six coupled equations:

$$\frac{\partial E_z}{\partial y} - \frac{\partial E_y}{\partial z} = j\omega\mu_0 H_x \tag{2.13}$$
$$\frac{\partial E_x}{\partial z} - \frac{\partial E_z}{\partial x} = j\omega\mu_0 H_y \tag{2.14}$$
$$\frac{\partial E_y}{\partial x} - \frac{\partial E_x}{\partial y} = j\omega\mu_0 H_z \tag{2.15}$$
$$\frac{\partial H_z}{\partial y} - \frac{\partial H_y}{\partial z} = -j\omega\varepsilon_0\varepsilon E_x \tag{2.16}$$
$$\frac{\partial H_x}{\partial z} - \frac{\partial H_z}{\partial x} = -j\omega\varepsilon_0\varepsilon E_y \tag{2.17}$$
$$\frac{\partial H_y}{\partial x} - \frac{\partial H_x}{\partial y} = -j\omega\varepsilon_0\varepsilon E_z \tag{2.18}$$

For propagation in the x-direction and homogeneity in the y-direction

$$\frac{\partial E_y}{\partial z} = -j\omega\mu_0 H_x \tag{2.19}$$
$$\frac{\partial E_x}{\partial z} - j\beta E_z = j\omega\mu_0 H_y \tag{2.20}$$
$$j\beta E_y = j\omega\mu_0 H_z \tag{2.21}$$
$$\frac{\partial H_y}{\partial z} = j\omega\varepsilon_0\varepsilon E_x \tag{2.22}$$
$$\frac{\partial H_x}{\partial z} - j\beta H_z = -j\omega\varepsilon_0\varepsilon E_y \tag{2.23}$$
$$j\beta H_y = -j\omega\varepsilon_0\varepsilon E_z \tag{2.24}$$

Combining 2.20, 2.22 and 2.24 one can achieve wave equation of H_y for Transverse Magnetic (TM) polarization.

$$\frac{\partial^2 H_y}{\partial z^2} + ({k_0}^2\varepsilon - \beta^2)H_y = 0 \tag{2.25}$$

Combining 2.19, 2.21 and 2.23 one can achieve wave equation of E_y for Transverse Electric (TE) polarization.

$$\frac{\partial^2 E_y}{\partial z^2} + ({k_0}^2\varepsilon - \beta^2)E_y = 0 \tag{2.26}$$

2.1.2 Surface plasmon polaritons at a dielectric-metal interface

Figure 2.1 depicts the simple geometry that can support surface plasmon polaritons at single interface. The solution for surface plasmon propagates along the interface and decays exponentially in the z-direction.

Figure 2.1: Geometry for surface plasmon polaritons at a dielectric-metal interface

We first investigate TM solutions:

for $z > 0$

$$H_y(z) = A_1 e^{j\beta x} e^{-k_1 z} \tag{2.27}$$

$$E_x(z) = \frac{j A_1 e^{j\beta x} e^{-k_1 z} k_1}{\omega \varepsilon_1 \varepsilon_0} \tag{2.28}$$

$$E_z(z) = \frac{-A_1 \beta e^{j\beta x} e^{-k_1 z}}{\omega \varepsilon_1 \varepsilon_0} \tag{2.29}$$

for $z < 0$

$$H_y(z) = A_2 e^{j\beta x} e^{k_2 z} \tag{2.30}$$

$$E_x(z) = \frac{-j A_2 e^{j\beta x} e^{k_2 z} k_2}{\omega \varepsilon_2 \varepsilon_0} \tag{2.31}$$

$$E_z(z) = \frac{-A_2 \beta e^{j\beta x} e^{k_2 z}}{\omega \varepsilon_2 \varepsilon_0} \tag{2.32}$$

Continuity of the tangential components along the interface gives $A_1 = A_2$ and,

$$\frac{k2}{k1} = -\frac{\varepsilon_2}{\varepsilon_1} \tag{2.33}$$

This requires that permittivities of region 1 and 2 should have opposite signs that means surface plasmons can exist at interfaces between materials with opposite signs such as metals and insulators. The solution for H_y should also satisfy the wave equation:

$${k_1}^2 = \beta^2 - {k_0}^2 \varepsilon_1 \tag{2.34}$$

$${k_2}^2 = \beta^2 - {k_0}^2 \varepsilon_2 \tag{2.35}$$

combining 2.33 2.34 and 2.35 we can obtain dispersion relation at a dielectric metal interface:

$$\beta = k_0\sqrt{\frac{\varepsilon_1\varepsilon_2}{\varepsilon_1+\varepsilon_2}} \tag{2.36}$$

For TE solutions:

for $z > 0$

$$E_y(z) = A_1 e^{j\beta x} e^{-k_1 z} \tag{2.37}$$

$$H_x(z) = \frac{-jA_1 e^{j\beta x} e^{-k_1 z} k_1}{\omega\mu_0} \tag{2.38}$$

$$H_z(z) = \frac{A_1\beta e^{j\beta x} e^{-k_1 z}}{\omega\mu_0} \tag{2.39}$$

for $z < 0$

$$E_y(z) = A_2 e^{j\beta x} e^{k_2 z} \tag{2.40}$$

$$H_x(z) = \frac{jA_2 e^{j\beta x} e^{k_2 z} k_2}{\omega\mu_0} \tag{2.41}$$

$$H_z(z) = \frac{A_2\beta e^{j\beta x} e^{k_2 z}}{\omega\mu_0} \tag{2.42}$$

Continuity of tangential components along the interface gives:

$$A_1(k_1 + k_2) = 0 \tag{2.43}$$

Since $k_1 > 0$ and $k_2 > 0$ this condition is satisfied when $A_1 = A_2 = 0$. Therefore surface plasmons are not supported for TE polarization.

2.1.3 Surface plasmon polaritons at multilayer systems

In this section we will investigate surface plasmon dispersion relation at multilayers as shown in Figure 2.2. In this system there are two interfaces separated from each other. If the separation is comparable to the decay length of surface plasmons, interactions between surface plasmons give rise to coupled modes. For TM polarization:

Figure 2.2: Geometry for surface plasmon polaritons at three-layer system

for $z > d/2$

$$H_y(z) = A_1 e^{j\beta x} e^{-k_1 z} \tag{2.44}$$

$$E_x(z) = \frac{j A_1 e^{j\beta x} e^{-k_1 z} k_1}{\omega \varepsilon_1 \varepsilon_0} \tag{2.45}$$

$$E_z(z) = \frac{-A_1 \beta e^{j\beta x} e^{-k_1 z}}{\omega \varepsilon_1 \varepsilon_0} \tag{2.46}$$

for $z < -d/2$

$$H_y(z) = A_3 e^{j\beta x} e^{k_3 z} \tag{2.47}$$

$$E_x(z) = \frac{j A_3 e^{j\beta x} e^{k_3 z} k_3}{\omega \varepsilon_3 \varepsilon_0} \tag{2.48}$$

$$E_z(z) = \frac{-A_3 \beta e^{j\beta x} e^{k_3 z}}{\omega \varepsilon_3 \varepsilon_0} \tag{2.49}$$

for $-d/2 < z < d/2$

$$H_y(z) = B_1 e^{j\beta x} e^{-k_2 z} + B_2 e^{j\beta x} e^{-k_2 z} \tag{2.50}$$

$$E_x(z) = \frac{-jB_1 e^{j\beta x} e^{k_2 z} k_2}{\omega \varepsilon_2 \varepsilon_0} + \frac{jB_2 e^{j\beta x} e^{-k_2 z} k_2}{\omega \varepsilon_2 \varepsilon_0} \tag{2.51}$$

$$E_z(z) = \frac{B_1 \beta e^{j\beta x} e^{k_2 z}}{\omega \varepsilon_2 \varepsilon_0} + \frac{-B_2 \beta e^{j\beta x} e^{-k_2 z}}{\omega \varepsilon_2 \varepsilon_0} \tag{2.52}$$

Continuity of tangential components along two interfaces gives:

at $z = d/2$

$$A_1 e^{-k_1 d/2} = B1 e^{k_2 d/2} + B2 e^{-k_2 d/2} \tag{2.53}$$

$$\frac{A_1 k_1 e^{-k_1 d/2}}{\varepsilon_1} = \frac{-B_1 k_2 e^{k_2 d/2}}{\varepsilon_2} + \frac{B2 k_2 e^{-k_2 d/2}}{\varepsilon_2} \tag{2.54}$$

at $z = -d/2$

$$A_3 e^{-k_3 d/2} = B1 e^{-k_2 d/2} + B2 e^{k_2 d/2} \tag{2.55}$$

$$\frac{-A_3 k_3 e^{-k_3 d/2}}{\varepsilon_3} = \frac{-B_1 k_2 e^{-k_2 d/2}}{\varepsilon_2} + \frac{B2 k_2 e^{k_2 d/2}}{\varepsilon_2} \tag{2.56}$$

The solution for H_y should also satisfy the wave equation:

$$k_1{}^2 = \beta^2 - k_0{}^2 \varepsilon_1 \tag{2.57}$$

$$k_2{}^2 = \beta^2 - k_0{}^2 \varepsilon_2 \tag{2.58}$$

$$k_3{}^2 = \beta^2 - k_0{}^2 \varepsilon_3 \tag{2.59}$$

Solving equations 2.53 to 2.59 results in an implicit expression for the dispersion relation of three layer system.

$$e^{-2k_2d} = \frac{k_2/\varepsilon_2 + k_1/\varepsilon_1}{k_2/\varepsilon_2 - k_1/\varepsilon_1}\frac{k_2/\varepsilon_2 + k_3/\varepsilon_3}{k_2/\varepsilon_2 - k_3/\varepsilon_3} \tag{2.60}$$

2.2 Finite-difference time-domain method

The finite-difference time-domain (FDTD) method is a general, straightforward implementation of Maxwell's equations in time domain for the solution of a variety of electromagnetic wave problems. The FDTD method is formulated by discretization of Maxwell's equations over a finite volume and and approximating the derivatives with central difference approximation.

Firstly, we will discretize scalar equation of Amperes law which involves partial derivative of electric field intensity(E_x) with respect to time at $t = n\Delta t$ and $z = k\Delta z$.

$$\sigma {E_x}^n(k) + \varepsilon\frac{{E_x}^{n+1/2}(k) - {E_x}^{n-1/2}(k)}{\Delta t} = -\frac{{H_y}^n(k+1/2) - {H_y}^n(k-1/2)}{\Delta z} \tag{2.61}$$

For the value of E_x at time step n, we have semi-implicit approximation:

$${E_x}^n(k) = \frac{{E_x}^{n+1/2}(k) - {E_x}^{n-1/2}(k)}{2} \tag{2.62}$$

By replacing this approximation for the equation above we have:

$$\sigma\frac{{E_x}^{n+1/2}(k) - {E_x}^{n-1/2}(k)}{2} + \varepsilon\frac{{E_x}^{n+1/2}(k) - {E_x}^{n-1/2}(k)}{\Delta t} = -\frac{{H_y}^n(k+1/2) - {H_y}^n(k-1/2)}{\Delta z} \tag{2.63}$$

$$(\frac{\sigma}{2}+\frac{\varepsilon}{\Delta t})E_x{}^{n+1/2}(k)=(-\frac{\sigma}{2}+\frac{\varepsilon}{\Delta t})E_x{}^{n-1/2}(k)-\frac{H_y{}^{n}(k+1/2)-H_y{}^{n}(k-1/2)}{\Delta z} \tag{2.64}$$

$$E_x{}^{n+1/2}(k)=(\frac{1-\Delta t\sigma/2\varepsilon}{1+\Delta t\sigma/2\varepsilon})E_x{}^{n-1/2}(k)-(\frac{2\Delta t}{(\Delta t\sigma+2\varepsilon)\Delta z})\frac{H_y{}^{n}(k+1/2)-H_y{}^{n}(k-1/2)}{\Delta z} \tag{2.65}$$

Secondly, we will discretize scalar equation of Faradays law which involves partial derivative of H_y with respect to time at t = (n +1/2) t and z = (k+1/2)z.

$$-\mu\frac{H_x{}^{n+1}(k+1/2)-H_x{}^{n}(k+1/2)}{\Delta t}=\frac{E_y{}^{n+1/2}(k+1)-E_y{}^{n+1/2}(k)}{\Delta z} \tag{2.66}$$

$$H_x{}^{n+1}(k+1/2)-H_x{}^{n}(k+1/2)=-(\frac{\Delta t}{\mu\Delta z})\frac{E_y{}^{n+1/2}(k+1)-E_y{}^{n+1/2}(k)}{\Delta z} \tag{2.67}$$

$$H_x{}^{n+1}(k+1/2)=H_x{}^{n}(k+1/2)-(\frac{\Delta t}{\mu\Delta z})\frac{E_y{}^{n+1/2}(k+1)-E_y{}^{n+1/2}(k)}{\Delta z} \tag{2.68}$$

These equations (2.65 and 2.68) can be directly implemented in a computer code. Once the spatial resolution Δz is chosen, the absolute size of the computational domain can be determined. While choosing the resolution it is necessary to have at least 10 cells per wavelength (smallest wavelength in the simulation) for an adequate simulation. Then, we can determine the time step necessary according to the spatial resolution. Finally, we should implement a cycle to compute the fields for a certain number of time steps.

2.3 Optical characterization of highly doped silicon

In order to determine optical properties of the highly doped silicon, Drude formalism is used:

$$\varepsilon(\omega) = \varepsilon_\infty(1 - \frac{{\omega_p}^2}{\omega(\omega + \frac{j}{\tau})}) \tag{2.69}$$

where ε_∞ is the permittivity value for $\omega >> \omega_p$ and taken as 11.7, τ is the relaxation time, ω_p is the plasma frequency:

$${\omega_p}^2 = \frac{Ne^2}{\varepsilon_0 \varepsilon_\infty m^* m_0} \tag{2.70}$$

where N is the free carrier concentration per cm^3, e is the elementary charge, $\varepsilon_0$is the vacuum permittivity, m^* is the effective mass, and m_0 is the electron mass.

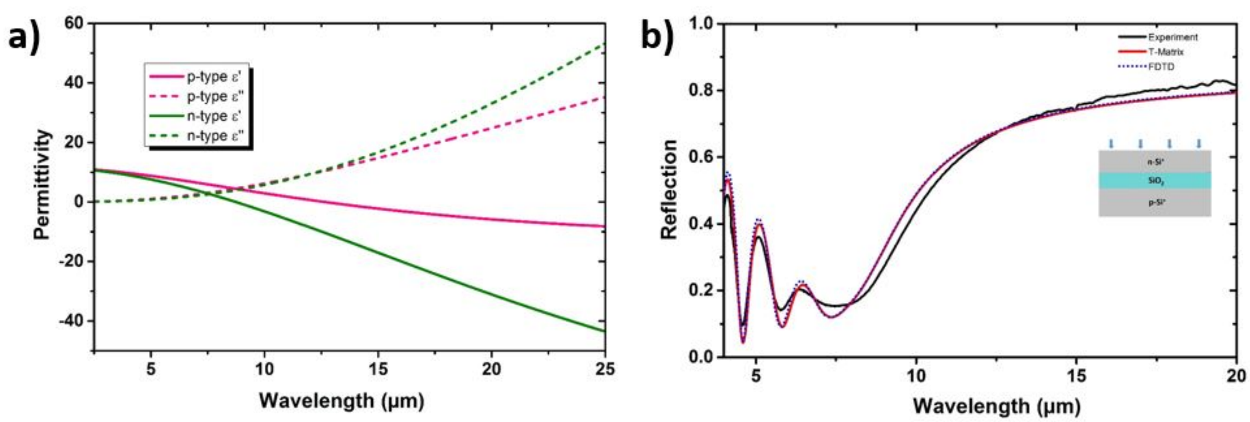

Figure 2.3: (a)Real and imaginary parts of the permittivity for heavily doped n-type and p-type silicon for top and bottom silicon layers of our structure.(b)Measured, simulated and analytically calculated (T-matrix) reflection spectrum of the SOI structure. Inset illustrates the SOI structure.

One of our substrates is a procured SOI wafer has n-type silicon layer at the top and p-type silicon layer at the bottom. Resistivity values of these silicon layers correspond to the doping density on the order of $N = 5 \times 10^{19} cm^{-3}$. In order to extract optical properties of the both n-type and p-type silicon layers we consider plasma frequency and relaxation time as our fitting parameters and we start calculations with $N = 5 \times 10^{19} cm^{-3}$ and $1/\tau = 0.037$ (eV) [19]. We optimized these parameters by fitting FDTD calculations to our experimental results. Eventually we obtained best fit for $N_n = 5.2 \times 10^{19} cm^{-3}$. and, $N_p = 5.5 \times 10^{19} cm^{-3}$. for n-type and p-type silicon layers, respectively. These carrier concentration values correspond to plasma wavelengths of $\lambda_n = 8.28 \mu m$ and $\lambda_p = 9.42 \mu m$ for n-type and p-type silicon layers, respectively. Figure 2.3a shows the modeled real and imaginary permittivity values of our n-type and p-type silicon layers. Figure 2.3b shows the measured, simulated and also analytically calculated (T-matrix formalism) reflection results of the SOI structure without patterning. In numerical calculations optical constants of silicon dioxide have taken from the literature [20]. As seen in this figure the numerical and the analytical reflection spectra fit very well to the experimental reflection spectrum indicating validity of our model.

Here we tried to extract optical properties by given approximate resistivity values (or approximate doping densities) and using a normal incidence reflection result. Even if we get a relatively consistent fitting results for this, there is more accurate method for this extraction, ellipsometry. Ellipsometry is a technique that is used to extract the optical constants of a material by measuring the change in the polarization of a light beam reflected from the material. In spectroscopic ellipsometry technique multiple measurements are taken for different incidence angles to increase accuracy. Figure 2.4 shows optical constants of a plain silicon wafer with a carrier concentration of 7×10^{19} fitted with spectroscopic ellipsometry.

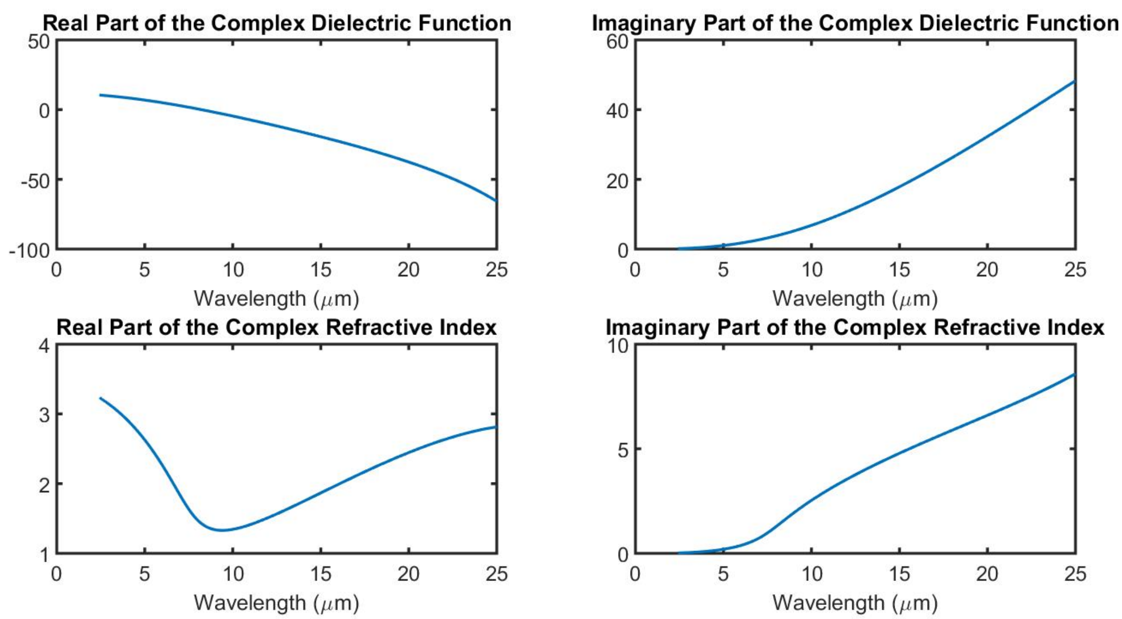

Figure 2.4: (a) Optical constants of a plain silicon wafer with a carrier concentration of 7×10^{19} fitted with spectroscopic ellipsometry.

Chapter 3

Ultra-Broadband infrared light absorption with patterned silicon-on-insulator (SOI) substrate

This chapter will be based on the publication "All-Silicon Ultra-Broadband Infrared Light Absorbers" K. Gorgulu et al., Scientific Reports, 6, (2016): 38589. Reproduced (or Reproduced in part) with permission from Nature Publishing Group. Copyright 2016 Nature Scientific Reports.

3.1 Introduction

By exploiting plasmonic structures, electromagnetic energy can be localized into a very small volume and efficient conversion between photons and plasmons can be controlled at sub-wavelength scale [21, 22]. Noble metals such as gold and silver are commonly used plasmonic materials at visible (VIS) and near-infrared (NIR) ranges. In order to exploit plasmonic enhancement in the mid-wave and long-wave infrared regions, materials with plasma frequencies in this range are required. Common metals have plasma frequencies in VIS and NIR regions. On the other hand, plasma frequency of semiconductors can be modulated by either changing charge carrier concentration (doping) or applying potential gating [14,23]. Therefore, highly doped semiconductors emerge as favorable alternatives of metals in plasmonics, especially in the infrared region. The performance of various semiconductor materials has been evaluated in a number of theoretical and experimental studies [24–27]. Among these semiconductors, silicon has attracted great interest due to silicon integrated photonic devices including subwavelength interconnects, modulators, and emission sources [23, 28]. Silicon also enables chip scale integration at mid-infrared (MID-IR) band where many potential applications arise including chemical and biological sensors, imagers, light sources and spectroscopy [29].

Demonstration of plasmonic effects by silicon in the infrared region is carried out by others [17, 18]. Several groups have studied silicon based surface plasmon resonances for bio-chemical sensing applications [30–32]. Frequency selective infrared absorbers have been proposed based on low-resistivity silicon gratings [33, 34]. For spectroscopy and imaging applications, it is highly desirable to have wideband absorbers. Most of the resonant absorbers suffer from narrow operating absorption waveband. Much of the work in this direction focuses on multi-resonance or tapered metamaterial structures to increase bandwidth [35–37]. One way of increasing absorption band is to use multilayered structures composed of lossy materials absorbing the light gradually. Recently, two studies were reported as in the form of a geometric transition absorber based on metal-dielectric slabs [36, 37]. Another approach is to combine different resonators to obtain wideband or multiband response [35, 38, 39]. However, as the number of resonators increases, so does the size of a unit cell, the fill factor and the absorption efficiency decrease. Therefore, highly efficient and ultra-wideband absorbers have not previously been proposed or implemented in the MID-IR region. In this study, we theoretically and experimentally demonstrate an ultra-wideband MID-IR absorber. Furthermore, we show that the absorption is related to the free carrier absorption, and vibrational and plasmonic resonances supported by the structure simultaneously. The absorber demonstrated in this study has an enhanced bandwidth without compromising absorption performance by alleviating the issues encountered in the previous studies presented in the literature. More importantly, proposed absorber is based on silicon and it extends silicon photonics to the mid-infrared wavelengths for optoelectronic systems. Such an absorber paves the way to the realization of all-silicon based sensors, imagers and spectroscopy applications, and provides chip-scale integration compatible with CMOS technology [40].

3.2 Methods

3.2.1 Device fabrication and measurement

Fabrication of our structures starts with commercial SOI wafers consisting of 500 μm thick highly doped handle layer silicon substrate at the bottom with resistivity range of $\rho = 0.002 - 0.005\Omega - cm$, 800 nm thick silicon dioxide in the middle and 2 μm thick highly doped device layer silicon at the top with resistivity range of $\rho = 0.001 - 0.0015\Omega - cm$. We first thinned the device layer silicon from 2 μm to 1.2 μm by using an SF_6 based isotropic RIE process. After thinning the device layer of the SOI to the desired thickness of 1.2 μm, we used standard photolithography procedures to define the desired patterns. First, we spun a positive photoresist (AZ 5214E) at 4000 r.p.m. and baked the photoresist at 110 °C for 50 seconds. Then, we exposed the photoresist with a contact aligner and developed the photoresist with DI water diluted AZ 400K developer. Using a BOSCH process recipe that is SF_6 based RIE at the etch step, and C_4F_8 based deposition at the passivation step, the 1.2 μm thick Si is patterned till the 800 nm silicon dioxide surface is reached. Then, the remaining photoresist is removed by an oxygen plasma cleaning recipe. Simple fabrication process shown in Figure 3.1. In order to measure the reflection of the fabricated structures, Bruker HYPERION 2000 IR microscope and Bruker Vertex 70v Fourier transform infrared (FTIR) spectrometer are used. The measurements are referenced to a gold-coated flat silicon mirror.

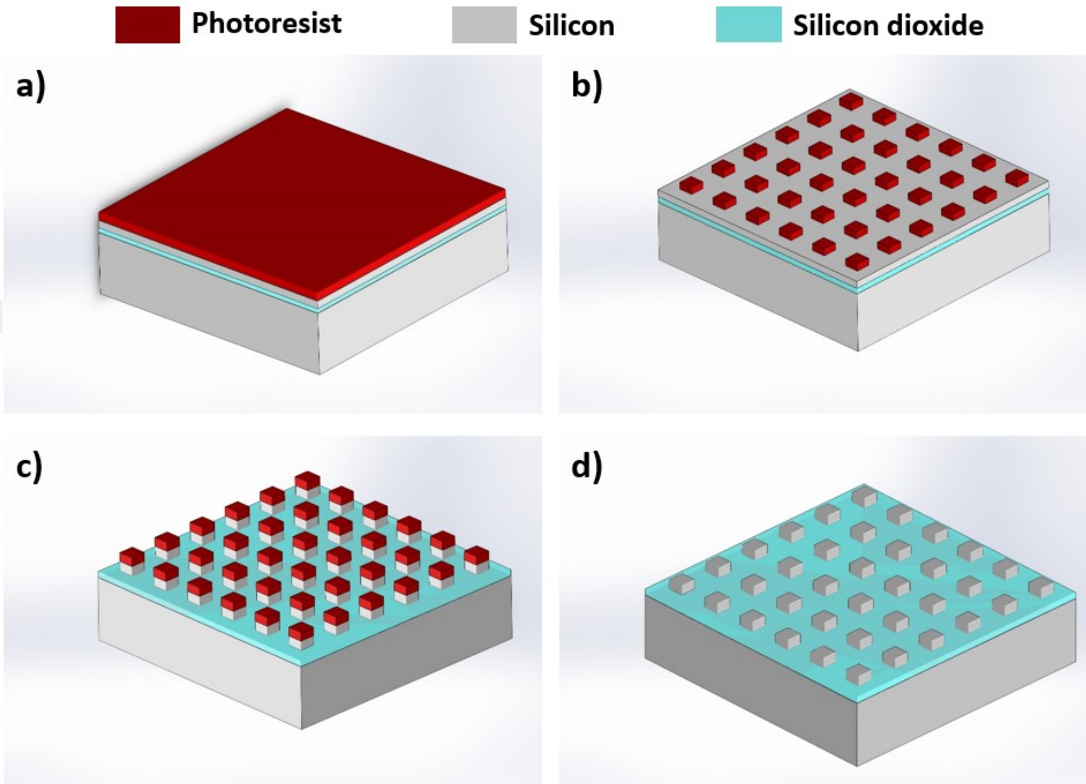

Figure 3.1: (a) Process flow for fabrication of silicon based 2D gratings utilizing SOI structure. First, 2.0 μm thick Si is thinned down to 1.2 μm Si. For simplicity, this step is not shown in the figure. After thinning the device Si layer, the rest of the patterning steps are explained in this illustration. (a) Spin coating of photoresist, (b) photolithography patterning, (c) etching of silicon by BOSCH process, (d) removal of photoresist with oxygen plasma.

3.2.2 Simulations

Electromagnetic wave simulations are performed using FDTD Solutions by Lumerical Inc, a commercially available FDTD simulation software package. For 3D simulation setup; on the x and y axes periodic boundary conditions are used, and on the z-axis (propagation direction) a perfectly matched layer (PML) is used. For 2D simulation setup; on the x-axis periodic boundary condition is used, and on the y-axis (propagation direction) PML is used. In all of the simulations, we employed cubic mesh with a mesh size of 10nm.

3.3 Results and discussions

Figure 3.2a presents the schematic diagram of the wideband absorber. The absorber is composed of a three-layer-stack of silicon-silicon dioxide-silicon structure. Only the top silicon layer is patterned periodically along both x and y directions. For the fabrication of the structures, a commercially available silicon-on-insulator (SOI) wafer is utilized. Conventional optical lithography and deep reactive ion etching (DRIE) techniques are used for the microfabrication of the structures. The thicknesses of the silicon grating and the silicon dioxide layer are h=1.2 μm and t=0.8 μm, respectively. Two structures with different periodicities, P=7 μm and P=8 μm, and different widths, W=3 μm and W=4.2 μm, are implemented. Figure 3.2b shows the scanning electron microscope (SEM) image of the sample with periodicity, P=8 μm.

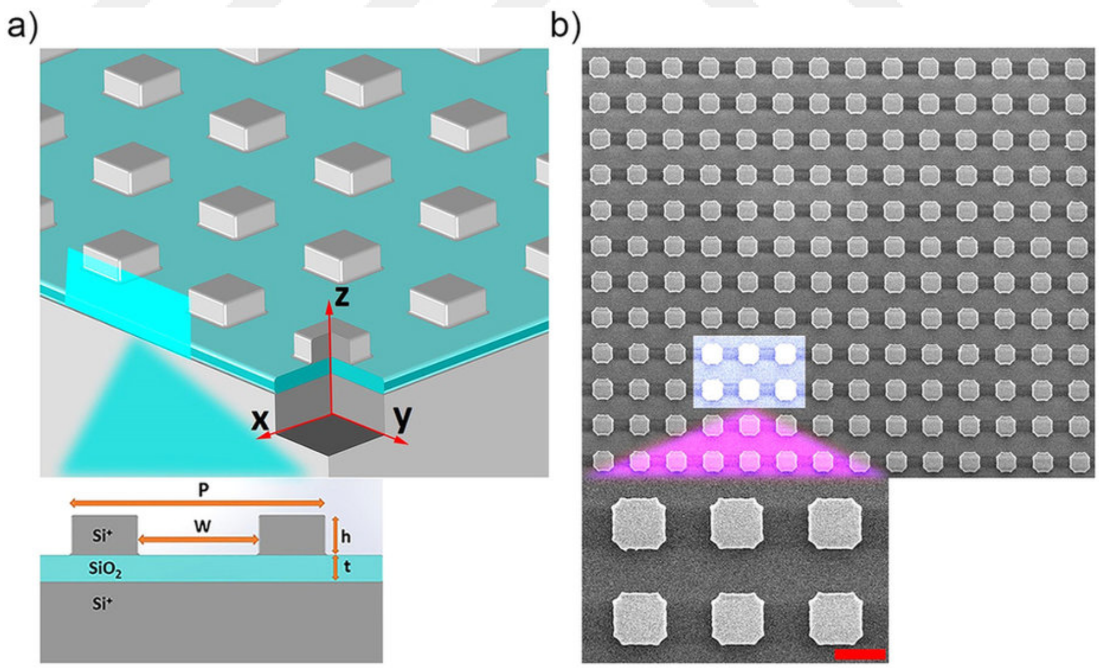

Figure 3.2: (a) Schematic representation of a three layer silicon-silicon dioxide-silicon structure with the top silicon layer patterned as 2D gratings of periodicity P, (b) SEM image of one of the fabricated samples with periodicity, P=8 μm. Scale bar is 4 μm.

In order to conduct numerical analysis of these structures, we used finite difference time domain (FDTD) method. Optical properties of highly-doped semiconductors are dominated by electron plasma of the material, and can be modeled using Drude formalism [17,18]. The optical properties of the top and bottom silicon layers are extracted using Drude formalism. Our model is confirmed by means of an experimental setup. Doping concentrations of the top (n-type) and bottom (p-type) silicon layers are found to be $N_n = 5.2 \times 10^{19} cm^{-3}$ and $N_p = 5.5 \times 10^{19} cm^{-3}$, respectively; and the relaxation frequencies are $\omega_n = 0.04eV$ and $\omega_p = 0.07eV$, respectively. A characteristic frequency of semiconductors is called plasma frequency, which is defined as the frequency at which the real part of the permittivity vanishes. Plasma wavelengths of the top and bottom silicon layers are extracted to be $\lambda_n = 8.28\mu m$ and $\lambda_p = 9.42\mu m$, respectively. In FDTD simulations optical constants of silicon layers are taken from Drude formalism results and the optical constants of silicon dioxide are received from the literature [20]. The absorption in the simulations is defined as $A(\lambda) = 1 - R(\lambda) - T(\lambda)$, where $T(\lambda)$ is the transmitted power and $R(\lambda)$ is the reflected power. Figure 3.3 shows the simulated reflection, transmission, and absorption spectra at normal incidence for arbitrarily polarized light. In these computational analyses, transmitted power is calculated at 2.5 μm below the interface between silicon dioxide and bottom silicon layer. Highly-doped silicon has a very high attenuation coefficient ($1.61\mu m^{-1}$ at plasma wavelength, $\lambda = 9.42\mu m$), therefore almost no power is transmitted through the structure beyond plasma wavelength and only a weak transmission is observed at shorter wavelengths from simulation results. Plasma wavelength of the bottom silicon layer can be shifted to shorter wavelengths by increasing the doping density which will further decrease the transmitted power. Two different samples with periodicities of 7 μm and 8 μm provide absorption waveband of 5-18.8 μm and 5.4-20 μm, respectively; yielding excellent absorption performance that is more than 90 % in average. Red lines in Fig. 3.3a-b show the corresponding experimental reflection results of these wideband absorber structures and the measured reflection spectra agree well with the simulated ones.

The effect of multiple resonances can be identified from the absorption peaks in the spectra. In order to understand the nature of absorption processes we

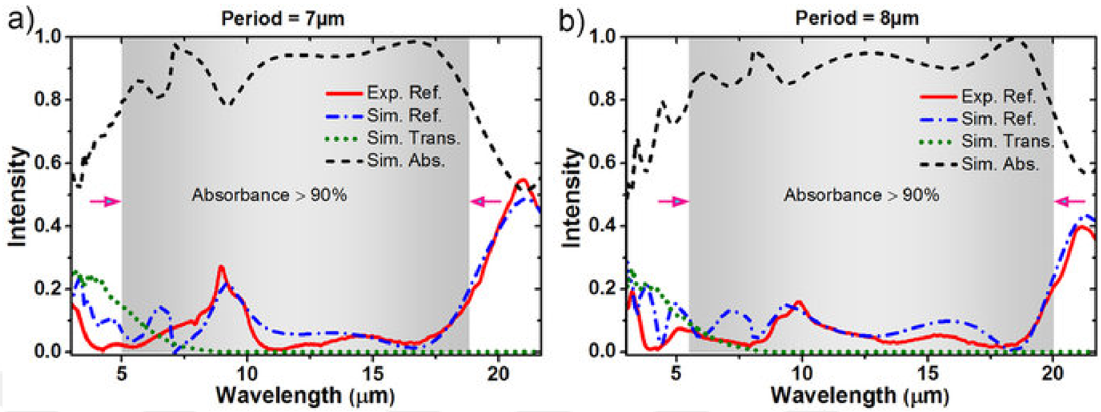

Figure 3.3: (a,b) Simulated reflection (Sim. Ref.), transmission (Sim. Trans.) and absorption (Sim. Abs.) spectra and measured reflection (Exp. Ref.) spectrum for the samples with periodicities of P=7 μm and P=8 μm.

first investigated the absorption properties of one dimensional (1D) 1.2 μm-thick silicon stripes on 0.8 μm-thick silicon dioxide spacer on silicon substrate. The periodicity and the fill ratio of the silicon stripe array are 8 μm and 0.5, respectively. Figure 3.4a shows the simulated normal incidence absorption spectra of this 1D structure for both TE (E-field is parallel to the silicon grating direction) and TM (E-field is perpendicular to the silicon grating direction) polarization configurations. For TE polarization, absorption between 6 μm and 9 μm is dominated by free carrier absorption in heavily doped silicon layers. This is the classical Drude absorption by free carriers and can be spectrally tuned by controlling the carrier concentration of silicon layers. Since the real part of the permittivity is very low around the plasma frequency, light can easily penetrate into the material. Therefore, reflection minimum and absorption maximum of a non-corrugated highly doped silicon occurs near the plasma frequency. Figure 3.5 shows the bulk absorption of the 4 m thick silicon with different doping concentrations. As it seen in the graph, absorption peak blueshifts as the concentration increases.

Around 10 μm, silicon dioxide exhibits molecular resonance due to Si-O-Si vibrations. Asymmetric stretching vibration of Si-O-Si bridges contributes to the absorption in this region [41]. At longer wavelengths, free carrier conduction dominates, thus the reflectivity increases and the absorption decreases. For TM polarization, absorption spectrum gives the evidence for the excitation of surface

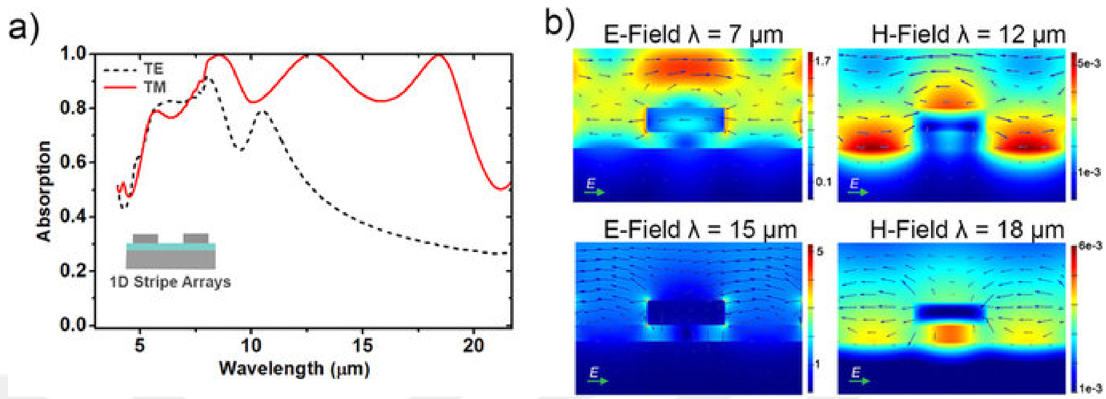

Figure 3.4: (a) Simulated absorption spectra of the 1D structure with periodicity 8 μm and fill ratio of 0.5 for TE and TM polarizations. Inset shows the schematic of 1D silicon silicon dioxide silicon structure (b) Calculated spatial field distributions for the same structure with periodicity of 8 μm at λ=7 μm, λ=12 μm, λ=15 μm, and λ=18 μm. The arrows represent the electric field vector.

plasmon modes. Two additional absorption peaks are observed at longer wavelengths (at 12.7 μm and 18 μm) in addition to the absorption bands at shorter wavelengths.

Additional information can be obtained from spatial field distributions. Figure 3.4b shows the calculated field distributions at four major points in the absorption spectrum of the structure with periodicity, P=8 μm using the FDTD method. The electric field at 7 μm is mainly concentrated on the top of the silicon grating, where incident field constructively interferes with the reflected field. At this range, field also penetrates through the silicon layers and is absorbed by free carriers. At wavelengths longer than the plasma wavelength, highly doped silicon layers behave like metals and the structure exhibits the properties of the common metal/insulator/metal (MIM) structures. Similar MIM structures consisting of a metal structure and a metal film separated by a dielectric layer were reported by several groups. These studies have shown the coupling between different plasmonic modes and investigated the effects of the structure periodicity, the fill ratio and the dielectric thickness on these plasmonic modes. When the periodicity of the structure is on the order of the wavelength, propagating surface plasmon resonances can be generated. The magnetic field distribution at 12 μm shows strong confinement at the top of the silicon gratings and between two adjacent gratings.

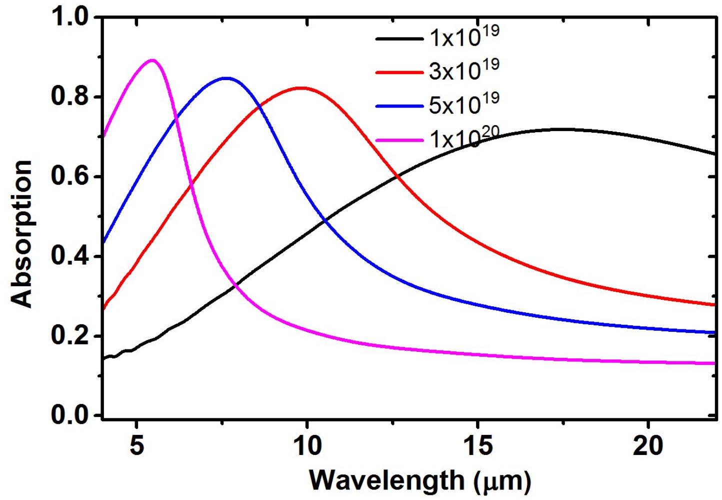

Figure 3.5: Simulated absorption spectra of 4 μm thick silicon with different doping concentrations.

The field distribution at this range confirms that the absorption at this point arises from grating induced silica-side propagating surface plasmons (PSP). On the other hand, magnetic field at 18 μm is concentrated below the silicon gratings, in the gap filled by silicon dioxide. The absorption peak at this point is due to the gap-plasmon (GP) modes supported by the cavity between silicon layers as reported for similar MIM structures [42–48]. Electric field distribution at 15 μm shows strong confinement at the top and bottom of the silicon grating. Both PSP and GP modes have broad absorption bands (more than 5 μm), hence both of these modes have partial effects on the absorption at 15 μm.

Dispersion relation of the surface waves supported by unpatterned Si-SiO2-Si-Air structure is calculated by using a bandstructure technique of the FDTD method. In this bandstructure technique we do a parameter sweep over the transverse wavevector and look for frequencies with strong resonances. Simulated dispersion relation of this multilayer system is shown in Fig. 3.6a. Two vibrational bands of silicon dioxide, located at 13.6 THz (22 μm) and 30 THz (10 μm) [41], can be observed. Analytical dispersion relation of Metal/Insulator/Metal like structures are reported previously [49, 50]. The transverse magnetic plasmon dispersion relation for an asymmetric MIM structure is given by,

$$e^{-2k_2 t} = \frac{k_2/\varepsilon_2 + k_1/\varepsilon_1}{k_2/\varepsilon_2 - k_1/\varepsilon_1} \frac{k_2/\varepsilon_2 + k_3/\varepsilon_3}{k_2/\varepsilon_2 - k_3/\varepsilon_3} \tag{3.1}$$

where ε_1, ε_2, and ε_3 represent the permittivities of the layers; bottom Si^+, SiO_2, and top Si^+, respectively. t is the gap thickness. k_1, k_2, and k_3 are the wavevectors perpendicular to the interfaces defined by momentum conservation:

$${k_i}^2 = {k_{spp}}^2 - {k_0}^2 \varepsilon_i \tag{3.2}$$

for i=1, 2, and 3. k_{spp} is the wavevector of the surface plasmons. Surface plasmon polariton dispersion relation at a single interface is given by [51]:

$$\beta = k_0 \sqrt{\frac{\varepsilon_1 \varepsilon_2}{\varepsilon_1 + \varepsilon_2}} \tag{3.3}$$

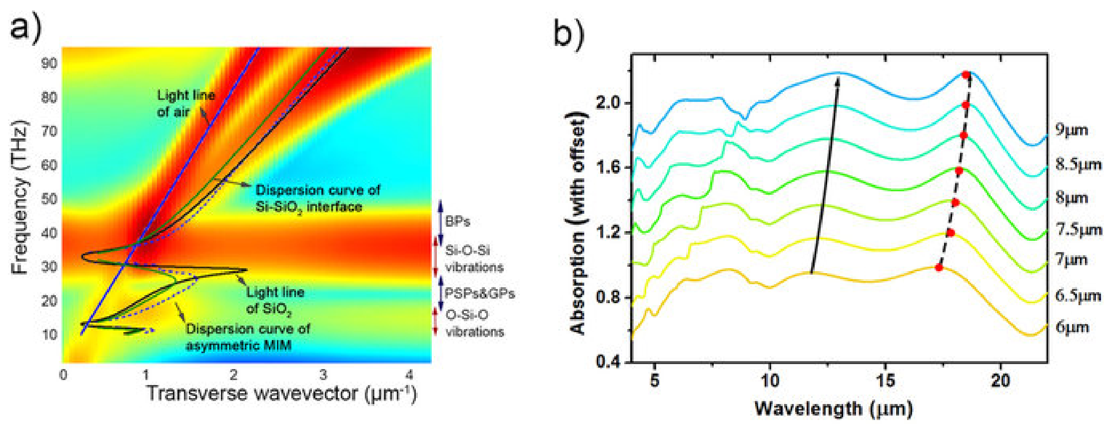

Figure 3.6: (a) Simulated and analytical dispersion relation for the silicon-silicon dioxide-silicon-air structure. Abbr: BPs (Bulk Plasmons), PSPs (Propagating Surface Plasmons), GPs (Gap Plasmons). (b) Dependence of the absorption spectrum on the structure periodicity. Fill ratio is kept constant as 0.5 and the periodicity is varied from 6 μm to 9 μm.

Dispersion relation of MIM systems are implicit functions and can be solved numerically. Dashed blue line in Fig. 3.6a show the theoretical result for the dispersion relation of silicon-silicon dioxide-silicon structure. Solid green line in the same figure represents the dispersion relation of propagating surface plasmons between silicon and silica. The plasmonic resonances, PSPs and GPs, are excited in the frequency range between the two vibrational bands of the silicon dioxide.

Figure 3.6b shows the simulated absorption spectra for various grating periodicities. In these simulations the fill ratio is kept constant as 0.5 and the periodicity is varied from $6\mu m$ to $9\mu m$. Both of the plasmonic resonances show redshift with increasing periodicity. PSP mode (solid black line) is excited by periodic nature of the structure, so the resonance wavelength redshifts with increasing periodicity as expected. However, the resonance shift of GP mode essentially depends on the width of the silicon gratings rather than the periodicity. The constructive interferences of GP mode, reflected back and forth at the edges of the cube, create a cavity resonance as in a Fabry-Perot interferometer. Therefore, the width of the silicon grating plays an essential role for the resonance shift as being a parameter of this cavity [42, 45, 47, 48]. GP resonance wavelength is related to the width of the silicon grating, w, by [42, 47, 49].

$$w\frac{2\pi}{\lambda}n_{eff} = m\pi - \varphi \tag{3.4}$$

where n_{eff} is the effective index of the gap and can be calculated from dispersion relation, m is the mode order and φ is the phase of the reflection coefficient of the mode at the end of the gap. The reflection phase φ, zero for a perfect Fabry-Perot cavity, is nonzero for a finite waveguide and depends on the structure and material properties [43, 48]. There is no analytical solution for reflection phase, hence it can be computed numerically or it is estimated as an average value minimizing the error of resonance wavelengths [42, 43, 47, 48]. In our structure we observe that the change in the reflection phase is nonsignificant when the fill ratio is kept constant. In order to determine reflection phase, we used one of the simulation results and we extracted the reflection phase as 63° according to the resonance wavelength in the simulation result. Since the reflection phase does not change significantly, all the other resonance wavelengths can be estimated accurately by Eq. 3.4 for the first order resonance (m=1). As shown in Fig. 3.6b the simulated resonance wavelengths (dashed black line) almost match up with semi-analytically calculated (red circles) ones with an error less than 0.5%.

We also investigated the performance of the structure with periodicity 8μm and fill ratio 0.5 for different doping concentrations. Figure 3.7a shows absorption spectrum as a function of doping density and wavelength. Dotted black line in the figure shows how plasma frequency shifts with increasing doping density. Due to the high penetration of field near the plasma frequency there exists an absorption band following the plasma frequency line. Plasmonic absorption bands (dashed white and dashed yellow lines) also shift to shorter wavelengths with increasing doping density. Blueshift of plasmonic absorption bands can be confirmed by dispersion relations. Increasing doping concentration shifts dispersion curves to higher frequencies, thus excitation of plasmonic resonances occurs at shorter wavelengths. The blue rectangle shows the doping concentration range where ultra-broad absorption band can be obtained for this structure. Doping concentrations of silicon layers in the experimental part fall into this region.

In order to enrich our study and investigate further the origin of the plasmonic resonances we conducted angle-dependent simulations using the FDTD method. Figure 3.7b shows the evolution of the absorption spectra with increasing incidence angle. As shown in the figure, one of the plasmonic modes redshifts with the increasing incidence angle. The dependence of the plasmonic mode on the angle of incidence indicates that this is a propagating mode. As this resonance point shifts to longer wavelengths, vibrational absorption band of silicon dioxide becomes discernable around 10 μm. On the other hand, the other plasmonic mode around 18 μm as being a GP mode is almost independent of the incidence angle of the light. This is in agreement with previous studies done on similar systems by other groups [42, 45, 48]. Nearly all broadband absorbers are designed to absorb light independent of polarization and angle of incidence. In order to achieve a polarization-independent electromagnetic response we design our structure to be symmetric in both x and y directions. Figure 3.7c shows the average absorption as a function of incidence angle for both TM (x-polarized, θ is in x-z plane) and TE (y-polarized, θ is in x-z plane) polarizations. At normal incidence,

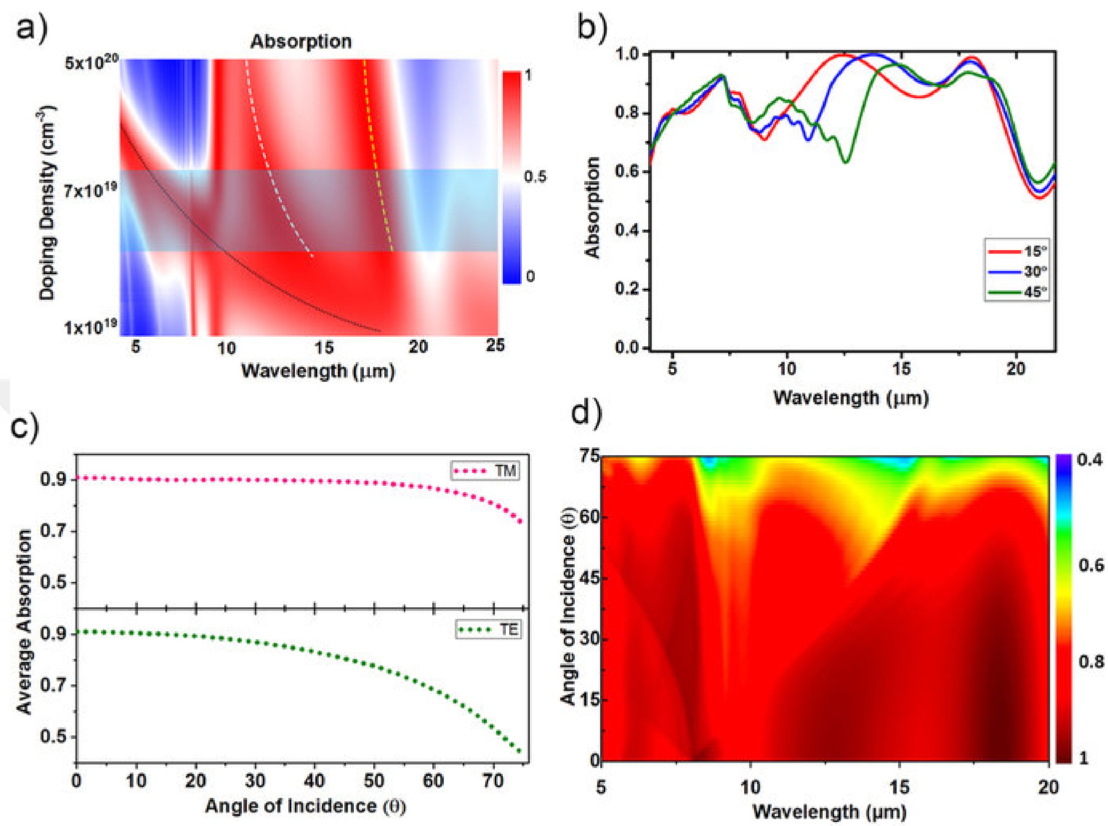

Figure 3.7: (a) Absorption spectrum as a function of wavelength and doping density. (b) Absorption spectrum of the structure with periodicity 8 μm and fill ratio 0.5 for three different incidence angles. The structure is illuminated by a TM polarized plane wave. (c) Average absorption as a function of angle of incidence for TM and TE polarizations. (d) Absorption spectrum as a function of wavelength and angle of incidence.

the absorption spectra for both polarizations are the same because of the symmetry in the structure. For TM polarization average absorption is above 80% even at 70° angle of incidence and then it decreases dramatically. For TE polarization absorption is maintained around 80% at up to 50° angle of incidence. Figure 3.7d shows the extinction spectra as a function of wavelength and angle of incidence for the light composed of both TM and TE polarization components. As it is seen in the figure, the broadband response is maintained when the incidence angle smaller than 50°, which is a significant achievement for resonant absorbers.

3.4 Conclusion

In conclusion, we have demonstrated ultra-broadband MID-IR absorbers on low-resistivity silicon. Periodically arranged silicon gratings are fabricated by using standard optical lithography and DRIE of silicon allowing for a cost-effective fabrication of micro-scale structures. Two different structures with periodicities of 7 μm and 8 μm provide average absorptivity of more than 90% in the waveband of 5-18.8 μm and 5.4-20 μm, respectively, with a total thickness less than the quarter of the wavelength. The structures also exhibit broadband absorption performance even at high angles of incidence (θ=50°) independent of the polarization. Our detailed analysis indicates that ultra-broadband light absorption originates from superposition of the free carrier absorption, and vibrational and plasmonic resonances excited at different portions of the MID-IR range. Silicon-based strong and ultra-broadband absorption of light at MID-IR region is very promising for realization of silicon based infrared imagers, sensors, and enhanced spectroscopy. Combined with extensive processing and device design knowledge base of silicon, presented absorbers yield fabrication simplicity and CMOS compatible optoelectronic integration.

Chapter 4

Silicon based plasmonic surfaces for sensing

This chapter will be based on the publication "High-conductivity silicon based spectrally selective plasmonic surfaces for sensing in the infrared region" K. Gorgulu et al., Journal of Optics, 19.2, (2016): 025002. Reproduced (or Reproduced in part) with permission from IOP Publishing.

4.1 Introduction

Plasmonic and metamaterial electromagnetic absorbers have attracted extensive attention not only for their fascinating electromagnetic properties, but also for their potential for various photonic applications. A perfect absorber absorbs all incident radiation at the frequency of operation by suppressing reflection, transmission and scattering in the structure. The first studies on metamaterial absorbers were in the microwave and THz regimes, utilizing two metallic layers separated by a dielectric layer [52–54]. Perfect absorption has been demonstrated with different types of unit cell structures such as patches, stripes and discs at these wavelengths. A downscaling of unit cell dimensions allowed practical perfect absorbers at mid-infrared, near infrared and visible wavelengths with very high absorption efficiencies [55–57].

Carefully designed sub-wavelength metallic structures provide excitation of plasmonic and photonic resonances that show narrow absorption bands. Researchers tried to increase the absorption waveband by exploiting multiple resonances simultaneously, for applications where broadband absorption is desirable [4, 58]. However, some other applications, such as selective thermal emitters and detectors, and bio-chemical and refractive index sensors, require narrow absorption bands [9,10]. Plasmonic absorbers typically have narrow resonance bands and therefore they can be utilized in spectrally selective detection schemes such as uncooled microbolometers [4]. According to Kirchhoff's law of thermal radiation, a perfect absorber is equivalent to a good thermal emitter. In order to get a sharp emissivity peak, a narrowband absorber is required. Narrow resonance bands are also highly desirable in sensing applications in order to detect minute changes in the environment. Plasmonic resonances, confined to a metal dielectric surface, are extremely sensitive to the refractive index of the surrounding dielectric medium. Such strong dependency on the refractive index of the surrounding dielectric medium paves the way for ultra-sensitive label-free refractive index sensing applications [11, 12].

All examples mentioned above utilize conventional metallic components, such as gold and silver, as their material building blocks. In commonly used metals, the magnitude of the real part of the permittivity is very large at mid-infrared wavelengths. This feature of metals significantly limits their plasmonic mode confinement in the mid-infrared regime [13]. Conventional metals such as Ag also pose fabrication challenges and have degradation problems on exposure to air or humidity, limiting fabrication and integration of devices [14]. On the other hand, highly doped semiconductors are shown to exhibit plasmonic behavior in the mid-infrared regime [17, 24, 26, 59]. Compared to their metallic counterparts, highly doped semiconductors provide enhanced device performance, and fabrication and CMOS integration feasibility. Due to silicon's prevailing manufacturing knowledge base, silicon plasmonics has received great attention. Localized surface plasmon resonances excited on silicon nanowires synthesized via the vaporliquid-solid technique have been demonstrated [30]. Infrared absorption performance of a one-dimensional (1D) silicon grating and its possible application as a biological sensor have been studied computationally [32, 33]. Also, surface plasmon based thermal emission from patterned silicon has been studied experimentally [60].

In this paper we numerically and experimentally demonstrate frequency selective infrared absorbers based on highly conductive silicon (p-type, $\rho = 0.001 - 0.002\Omega - cm$). Furthermore, we demonstrate that the designed plasmonic devices are promising as efficient refractive index based sensing surfaces. We also study the dependence of sensing performance of our structure on the doping concentration of silicon [61].

4.2 Structure and methods

Figure 4.1a presents a schematic representation of the proposed structures. Two-dimensional (2D) grating structures were patterned on a highly conductive silicon wafer using standard photolithography and reactive ion etching (RIE) techniques. First, we spun a photoresist, AZ 5214E at 4000 rpm, and baked it at 110 °C for 50 s. Then, we exposed the photoresist to a contact aligner and developed the photoresist with a deionized water diluted AZ 400 K developer. Silicon was patterned using a BOSCH process recipe that is SF_6 based RIE at the etch step, and C_4F_8 based deposition at the passivation step. Then, the remaining photoresist was removed by an oxygen plasma cleaning recipe. Two structures with different periodicities, P = 8 μm and P = 9 μm, and different widths, W = 5.2 μm and W = 5.85 μm, were made. The height of the gratings is 1.4 μm. A top view scanning electron microscope (SEM) image of the 2D silicon absorber with periodicity P = 8 μm is shown in figure 4.1b. Reflection spectra from the fabricated samples were obtained using a Bruker HYPERION IR microscope and Bruker Vertex 70v Fourier transform infrared (FTIR) spectrometer with a gold mirror as the calibration reference.

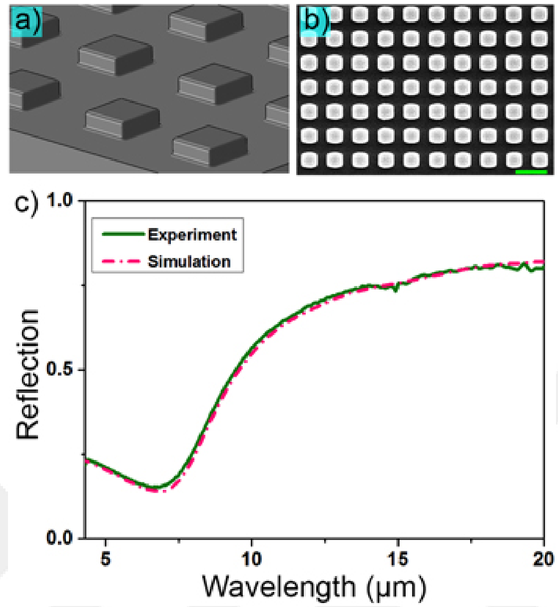

Figure 4.1: (a) Schematic illustration of 2D grating structures. (b) Top-view scanning electron microscope image of the 2D plasmonic absorber structure with periodicity of P = 8 μm and fill ratio of 0.65. Scale bar is 10 μm. (c) Measured and simulated reflection from the flat silicon surface.

Optical properties of the highly conductive silicon can be modeled using the Drude formalism considering carrier density and mobility as the fitting parameters of the material [19,27]. According to the model, carrier density and mobility of highly doped silicon used in this study were $7.5 \times 10^{19} cm^{-3}$ and $51 cm^2 V^{-1} s^{-1}$, respectively. There is a characteristic transition wavelength called plasma wavelength which is defined as the wavelength at which the real part of the permittivity vanishes. The plasma wavelength of highly doped silicon substrates used in this study was calculated to be $\lambda_{pl} = 8.2 \mu m$. At wavelengths longer than the plasma wavelength, the real part of permittivity becomes negative and highly doped silicon behaves like a metal. Therefore, surface plasmons can be excited in this regime.

Electromagnetic wave simulations were performed using the finite difference time domain (FDTD) method by Lumerical Inc., a commercially available FDTD simulation software package. A three dimensional (3D) simulation setup is used;

on the x and y axes periodic boundary conditions are used. On the z-axis (propagation direction) a perfectly matched layer (PML) is used. In all of the simulations, we employ a cubic mesh with a mesh size of 10 nm.

We performed simulations and experiments for the reflection behavior of a flat silicon surface. The reflectance results from the simulation and experiment for a flat surface are given in figure 1(c). The simulation result and experimental measurement are in good agreement. The reflection results presented in figure 4.1c are also confirmed by analytical reflection calculations obtained by Fresnel's equation.

4.3 Results and discussions

3D structures used in the FDTD simulations were imported from digitized SEM images of experimentally obtained 2D gratings. Figure 4.2a shows the calculated and measured reflection spectra of the 2D plasmonic absorber structures for arbitrarily polarized light at normal incidence in the wavelength range from 7 μm to 20 μm. The 2D surface pattern gives a polarization insensitive optical response. The measured reflection spectrum for the 2D grating with period P = 8 μm shows approximately 98% absorption at the resonance wavelength. Such a near perfect absorption can be ascribed to efficient coupling of incident light into surface plasmon modes through momentum matching by diffraction. Considering normal incidence, in such grating structures the plasmon wavevector, is generally determined by the Bragg vectors associated with the grating periodicities. However, because the structure dimensions are close to the wavelength of operation, resonance wavelength can be modified by the height and width of the gratings. As reported in a previous study, increasing the height of the grating leads to redshift in the resonance wavelength [60]. Structures with grating periodicities of 8 μm and 9 μm have reflection dips at 11.5 μm and 12.5 μm, respectively. Figure 4.2b shows a time-averaged magnetic field map for the structure with periodicity P = 9 μm at the resonance wavelength. As shown in the figure, magnetic field is strongly concentrated within the air trench surrounded by three highly doped siliconair interfaces. Figure 4.2c shows the time-averaged power flow distribution. The excitation of plasmonic resonance allows penetration of light into highly doped silicon and leads to strong optical absorption.

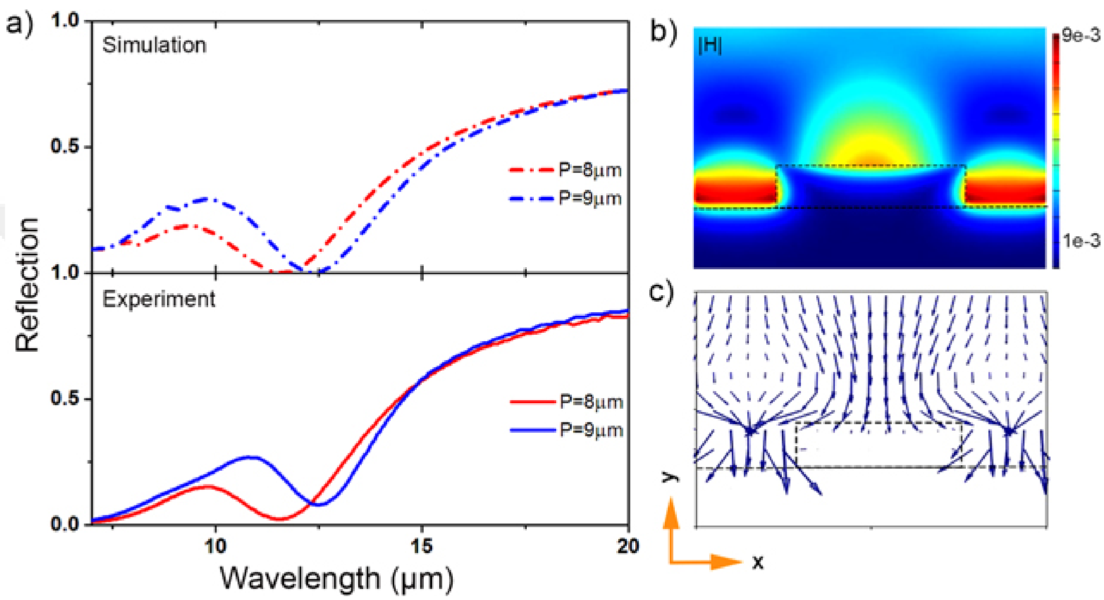

Figure 4.2: (a) Simulated and measured reflection spectra for structures with periodicities of P = 8 μm and P = 9 μm, and fill ratio of 0.65 for both structures. (b) Cross section of the time-averaged magnetic field for the structure with periodicity P = 9 μm at the resonance wavelength. (c) Cross section of the time-averaged optical power flow vector distribution.

Angular reflection measurements were obtained using a J A Woollam IR-Vase spectroscopic ellipsometer. The optical response of the plasmonic absorbers for different angles of incidence were also calculated with the FDTD technique. Figure 4.3 shows the reflection spectra for a 1D periodic sample in the case of three different angles of incidence. Simulated (dashed lines) reflectance spectra for the structures are in spectral agreement with experimental results (solid lines), but there are amplitude variations between measurement and experiment. For the simple 1D grating of grooves, phase-matching takes place whenever the condition $\beta = ksin\theta + \nu k_x$ is fulfilled, where k is the wavevector of the light incident at an angle θ, and $\nu = (1, 2, 3...)$. Therefore, increasing the angle of incidence redshifts the resonance wavelength. When the period increases, the effect of the reciprocal vector reduces. Hence, angular sensitivity increases with increasing structure period.

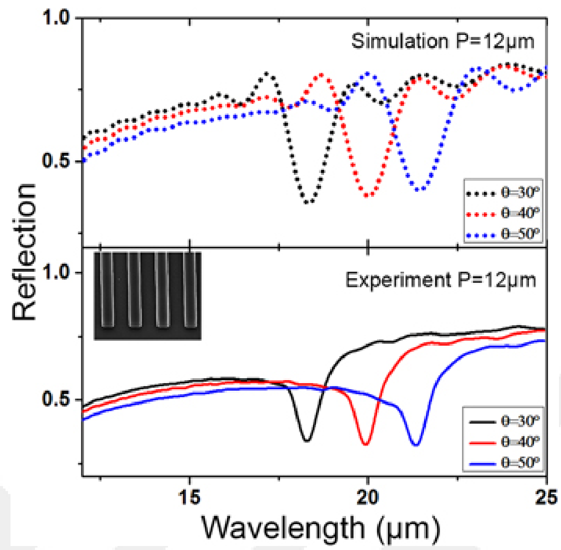

Figure 4.3: Simulated and measured reflection spectra at three different incidence angles for the structure with P = 12 μm, fill ratio of 0.45 and height of 1.4 μm. The inset shows the fabricated 1D device structure.

We investigated the refractive index sensitivity of our plasmonic absorber structures by immersing the structure with periodicity P = 9 μm in acetone and measuring the reflection spectrum. In the sensing experiments, the liquid film thickness of acetone is about 200 μm (which is much greater than the penetration depth of surface plasmons into the material above the silicon surface [17]). The sensitivity of a surface plasmon resonance based sensor is defined as the change in resonant wavelength as a function of change in refractive index, $S = \Delta\lambda/\Delta n$ nm/RIU. Since it is easier to detect resonance changes with narrow lines, the sensitivity is divided into full-width at half-maximum (FWHM) to determine the figure of merit, FOM = S/FWHM. Figure 4.4a shows reflection spectra for the same structure in two different media, air and acetone, and the infrared reflection spectrum of acetone. The refractive index of acetone is taken as 1.35 [62]. However, acetone has several molecular resonances over the entire mid-infrared region and the refractive index of acetone is modified in the vicinity of these resonance regions. In order to eliminate the effect of these resonances, reflection measurements of the plasmonic absorber under acetone are normalized to the infrared reflection spectrum of pure acetone. After normalization, molecular resonances of acetone are alleviated but they are still discernable in the spectrum.

However, line-widths of these resonances are much smaller than the line-widths of the plasmonic resonances. Therefore, plasmonic (indicated by blue arrows) and molecular (indicated by red arrows) resonances can be distinguished easily. We also simulated the reflection spectra for different refractive indices of the surrounding medium (Figure 4.4b). As depicted in figure 4.4b, the reflection spectrum shows a gradual redshift with increasing refractive index values. Both measured and simulated resonance wavelengths as a function of refractive index of the surrounding medium are given in figure 4.4c. According to the linear fitting of the resonance frequencies, the sensitivity value is found to be approximately 11 000 nm/RIU. Using this sensitivity value, the FOM value is calculated as 2.5. In general, the sensitivity of refractive index sensors is proportional to the operation wavelength. Therefore, the sensitivity of our absorber is very high compared to previous studies presenting their results at visible or near infrared regions [10, 12, 63–65]. However, in order to have a high FOM, the line-width of the resonance should be as small as possible. Even if our absorber has improved sensitivity, it has relatively low FOM values compared to the literature. It is important to note that reports of refractive index sensing applications on using conventional metals typically utilize either e-beam lithography or focused ion beam patterning. These techniques are costly and time-consuming for the fabrication of large-scale structures. Therefore, 1X contact photolithography and reduction photolithography based wafer scale fabrication of our silicon based sensors are promising for cost-effective applications.

The real and imaginary parts of dielectric permittivity of a semiconductor increase with doping concentration. Therefore, optical properties of a semiconductor become similar to those of traditional metals as the impurity concentration increases. We extracted optical properties of doped silicon using the Drude formalism for doping values from $4 \times 10^{19} cm^3$ to $5 \times 10^{20} cm^3$. We considered the dependence of mobility on the carrier concentration in calculations of the optical constants [66]. We investigated the dependence of the sensing performance on the doping density of silicon. We performed FDTD simulations for the same structure with different doping densities and two different refractive indices of the surrounding medium, n = 1 and n = 1.2. Figure 4.5a shows the simulated

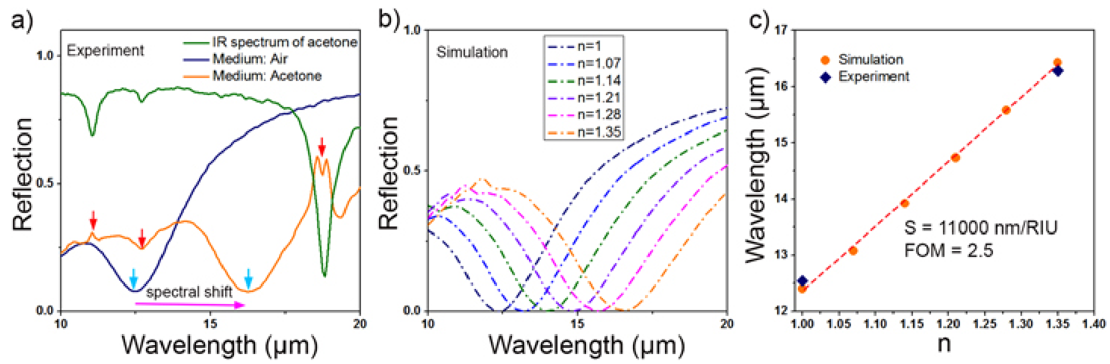

Figure 4.4: (a) Measured reflection spectra of the structure with periodicity P = 9 μm in two different media. Red arrows show the molecular resonance points of the acetone. Blue arrows show the plasmonic resonances of the patterned silicon under air and acetone. (b) Simulated reflection spectra for different refractive indices of the surrounding medium. (c) Measured and simulated resonance wavelengths as a function of refractive index of the surrounding medium.

reflection spectrum as a function of doping density for the structure with air as the surrounding medium. As is seen in the figure, as the doping density increases, the resonance band becomes narrower and resonance wavelength shifts to shorter wavelengths (indicated by the dashed line). As the doping concentration increases, the plasma frequency shifts to shorter wavelengths, surface plasmon dispersion curves also shift to higher frequencies. Figure 4.5b shows the sensitivity and FOM as a function of doping density. There is no significant change in the sensitivity, but the FOM increases with increasing doping density. As the doping concentration increases, the imaginary part of the dielectric function increases and the loss tangent decreases. These changes in the optical properties make the resonance band narrower [67], thus FOM and the sensing quality increase. A FOM value of 5.7 is obtained when the doping density is $5 \times 10^{20} cm^3$, and this value is greater or comparable to previously reported values obtained from various plasmonic structures [64, 68, 69].

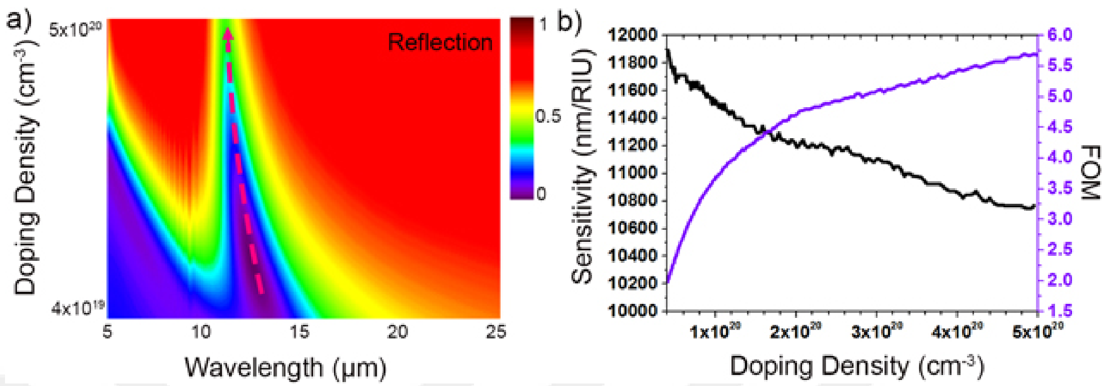

Figure 4.5: Reflection spectrum as a function of doping density for the structure with periodicity P = 9 μm and fill ratio of 0.65. (b) Calculated sensitivity and FOM as a function of doping density.

4.4 Conclusion

In summary, we have demonstrated all-silicon plasmonic absorbers with excellent absorption performances. Periodic silicon gratings were fabricated by scalable and cost effective methods including conventional photolithography and reactive ion etching techniques. We showed the spectral dependence of the resonance wavelength on the period of the structure and we studied the incidence angle behavior of the resonance wavelength. We further demonstrated the refractive index capability of silicon absorbers and showed a sensitivity of 11 000 nm/RIU and FOM value of 2.5. We also showed that the resonance waveband decreases as the doping density increases, thus sensing quality increases. In light of their ease of fabrication, silicon based plasmonic absorbers are highly advantageous for refractive index sensors.

Chapter 5

Fabrication and optical modeling of black silicon for mid-infrared light applications

This chapter will be based on the publication “Wideband ‘black silicon’ for mid-infrared applications” K. Gorgulu et al., Journal of Optics, 19.6, (2017): 065101. Reproduced (or Reproduced in part) with permission from IOP Publishing. Copyright 2017 IOP Publishing.

5.1 Introduction

Electromagnetic (EM) wave absorbers are of great importance for their potential of various applications including chemical and biological sensors, imagers, emission sources, and light harvesting devices. Considerable recent research has focused on increasing the efficiency of energy absorption processes. Highly efficient light absorption in metallic structures has been widely studied in metalinsulatormetal structures, nanoparticles, and arrays of metallic gratings [4, 58, 70–72].

Metamaterial absorbers are also widely explored as promising candidates to enhance EM wave absorption at microwave, terahertz, infrared, and visible frequencies [5–8]. However, confined by resonance nature of the unit structures, these metamaterial absorbers generally absorb light within a narrow wavelength range. Much of the work in this direction focuses on multi-resonance or tapered metamaterial structures to increase bandwidth. Nevertheless, the number of resonators combined within the same unit cell is limited. Moreover, these devices are typically made of metals that are not compatible with CMOS processes (such as Au) and that have degradation problem upon exposure to air and humidity such as Ag.

Alternatively, there are many materials, other than conventional metals, that provide advantages in device performance, integration, and tunability such as semiconductors, transparent conducting oxides, metal nitrides, perovskite oxides, silicides, germanides, and 2D materials [13, 14]. Among these materials, semiconductors have attracted great interest due to their well-established fabrication and integration technology. To date, various plasmonic and metamaterial absorbers have been studied with different semiconductors [15,25,30,73–76]. All-silicon efficient narrowband and broadband absorbers have been studied recently [27,40,61]. In addition to these absorbers, needle-like black silicon structures emerged as interesting material with broadband absorbance of more than 99% [77,78]. Several methods are used to obtain black silicon including chemical etching, (deep) reactive ion etching, and laser treatment [79]. So far black silicon structures are presented in the visible and the near-infrared region mostly for photovoltaic and surface enhanced sensing applications [80–82].

In this work, we investigate the absorption properties of black silicon in the mid-infrared region [83]. The starting substrate is a 7.5×10^{19} boron-doped (0.001-0.002 Ω cm) Czochralski-grown silicon wafer with the thickness of 500+/20 μm and ¡100¿ orientation. We use scanning electron microscope (SEM) images of the resulting silicon surface and implement the pattern into simulation environment. Furthermore, we use effective medium theory (EMT) to explain interaction of EM wave with black silicon structure. The absorption waveband of black silicon texture is significantly improved compared to that of flat silicon surface. Here, black silicon texture with random pyramidal structures acts like an antireflective coating and absorbs the incoming light by virtue of its high attenuation coefficient (1.7 μm^{-1} around plasma frequency). Classical antireflective designs for broadband operation typically have several thick layers [84]. However, this has the undesirable effect of making the structure bulky. Also, thick layers may cause delaminating of the deposited AR coating [85]. On the other hand, etched mechanical surfaces, like black silicon texture, can provide very broadband antireflective operation without such problems [86]. Broadband operation of black silicon texture can also be fine-tuned by controlling the shape of the individual features and conductivity of the silicon wafer. The mature silicon manufacturing technology could pave the way for CMOS compatible integration for specific applications.

5.2 Structure and methods

Optical properties of low resistivity semiconductors are dominated by electron plasma of the material, and can be modeled using Drude formalism. In order to extract optical properties of the highly doped silicon, we consider plasma frequency and relaxation time as our fitting parameters.

A p-type commercial silicon wafer was used as a starting substrate to obtain black silicon texture. The randomly distributed needle-like nanostructures were obtained across the full wafer using a Bosch process consisting of cyclic steps. Each half cycle consists of (i) 10 s SF_6 + O_2 gas mixture based reactive ion etching (RIE), and (ii) 7 s C_4F_8 based deposition (passivation step), respectively. The etching process was carried out using an STS Multiplex ICP Etch system. Gas flow rates for SF_6, C_4F_8, and O_2 were 80 sccm, 70 sccm, and 5 sccm, respectively. The platen temperature was kept constant at 20 C to fix the Si substrate temperature during the etching and deposition processes. The chamber pressure during etch step was kept constant at 35 mTorr. Similarly, the chamber pressure was kept constant at 20 mTorr during the deposition step. During the etch step, the coil power was set to 500 Watts, and platen power was set to 13 Watts. During the deposition step, the coil power was set to 400 Watts, and platen power was set to 0 Watts. Figure 5.1a shows two SEM images of one of the samples that is fabricated with 42 cycles of Bosch process. The top SEM image in figure 5.1a shows a sample whose middle section was intentionally removed out with focused ion beam milling in order to easily analyze the etching depth and texture of fabricated black silicon.

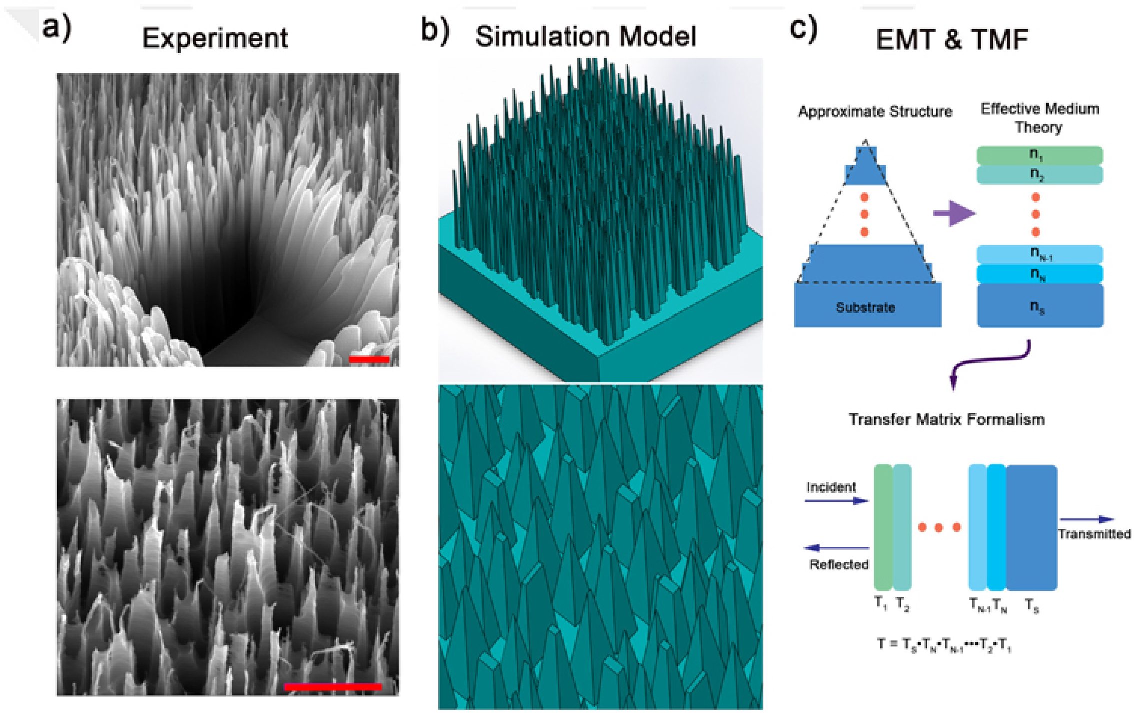

Figure 5.1: (a) SEM images of one of the fabricated samples. Scale bars are 1 μm (b) implementation of black silicon structure into the simulation environment. (c) Structural approximation of black silicon, effective medium theory (EMT) for this structure, and transfer matrix formalism (TMF).

Due to random nature of black silicon texture, numerical simulations were conducted with approximate models of black silicon. In this work, structures on the black silicon sample were very similar to pyramidal structures as shown in the SEM images in figure 5.1a. Therefore, we modeled black silicon structures as random pyramidal structures in simulation environment (figure 5.1b). We used an image processing software in order to determine the size distribution of the black silicon needles. EM wave simulations were performed using the finite difference time domain (FDTD) method. Three-dimensional simulation setup is constructed; on the x-axis and y-axis, periodic boundary conditions are used. On the z-axis (wave propagation direction) perfectly matched layer boundary condition is used. In all of the simulations, we employ cubic mesh with a mesh size of 10 nm.

Fabricated black silicon structures have pyramidal shapes with couple of micrometers in height, and couple of hundred nanometers (100-300 nm) in width. The widths of the structures are much smaller than the target wavelength range (5-10 μm). When EM wave interacts with structures much finer than its wavelength, rather than diffracting, it just reflects and transmits as if it is encountering a uniform medium [87]. Interaction of EM wave with such subwavelength structures can be described accurately by the EMT. We used MaxwellGarnett effective medium approximation in this study [88]:

$$\varepsilon = \varepsilon_0 \frac{f_0 \sigma(\varepsilon_m - \varepsilon_0) + \varepsilon_m + \sigma\varepsilon_0}{\varepsilon_m + \sigma\varepsilon_0 - f_m(\varepsilon_m - \varepsilon_0)} \tag{5.1}$$

where, ε is the effective permittivity of the medium, ε is the permittivity of free space, σ is the screening parameter, ε_m is the permittivity of the material, and f_m is the fill ratio. In effective permittivity calculations, we used Drude model results for ε_m. Screening factor depends on the geometry of the structure and it can be approximated as unity for the structures with high aspect ratio as in our case. As shown in the fabricated samples, fill ratio of the black silicon texture gradually increases from top to the bottom. Therefore, in order to describe the structure we used multi-level profile as shown in figure 5.1c. Each level has different fill ratio, and thus different effective permittivity. Consequently, we can model black silicon texture as a combination of uniform film stacks, each having finite film thickness. Finally the reflection and absorption of this multi-film structure can be calculated analytically by transfer matrix formalism (TMF).

5.3 Results and discussions

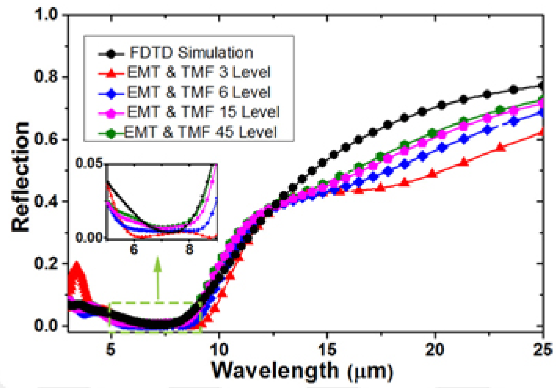

Figure 5.2: Simulated and analytically calculated reflection spectra of highly doped silicon with 7.5×10^{19} doping concentration, fill ratio 0-0.6. Analytical calculations conducted for different approximation levels.

We first compare the simulated and the analytical reflection results. We extract the optical constants of a flat silicon wafer for simulations and analytical calculations. For the characterization of the optical properties of the silicon wafer J A Woollam IR-Vase Spectroscopic Ellipsometer is used. Ellipsometric data is modeled with Drude formalism to extract optical constants. We used periodic pyramidal structures with height of 3.5 μm on average. Periodicity of the unit cell is taken as 1500 nm and fill ratio of the structure is varied from 0 (at the tip of the pyramids) to 0.6 (at the bottom of the pyramids). Using the optical properties obtained from ellipsometric measurements, FDTD simulations were conducted. In order to conduct analytical calculations we first represent our structure as an effective film stack. Here the structure is approximated as N-level profile as illustrated in figure 5.1c. The structure with height of 3.5 μm is divided into N layers where each layer has the same thickness (3.5/N) but different fill ratio. Using the extracted optical constants of silicon we calculated the effective complex permittivity of the layers considering their fill ratio as a parameter in the Maxwell-Garnett effective medium approximation. Finally, the reflection and the transmission are calculated by TMF using the calculated complex permittivity values. Figure 5.2 shows simulated reflection and analytical calculations with 3-level, 6-level, 15-level, and 45-level approximations to the structure. As the number of divisions (levels) increases the profile of the theoretical model better resembles the simulated structure, thus the calculated reflection spectrum approaches to the simulated reflection spectrum. The MaxwellGarnett effective medium approximation is valid for systems with low volume fractions [89]. In our case, fill ratio of the structure increases from top to bottom, thus the accuracy of the Maxwell-Garnett approximation is low at the bottom of the structure. The small difference between the analytical model and computational results is attributed to the Maxwell-Garnett effective medium approximation errors caused by relatively high volume fractions of the structure at the bottom.

Semiconductors are engineered materials and their optical properties can be tuned by controlling their carrier concentrations. Recently, active or passive tunable engineered semiconductor devices have been studied. Active tuning can be achieved by potential gating, while passive tuning can be achieved by doping [23, 90, 91]. Optical properties of highly doped silicon are dominated by different factors at low and high frequency limits. At low frequencies, as $\omega \tilde{\rightarrow} 0$, $1/\omega$ term dominates in the Drude model and imaginary part of the permittivity increases. Therefore, in low frequency regime, material behaves like a conductor. At high frequencies, $1/\omega^2$ term dominates in the Drude model and imaginary part of the permittivity decreases. Therefore in the high frequency regime, highly doped silicon behaves like low loss dielectric. Between low and high frequency regimes there is a characteristic transition frequency called plasma frequency at which material's optical response changes from dielectric to metallic. At the plasma frequency, the real part of the permittivity vanishes, but the imaginary part of the permittivity is still finite. Figure 5.3a shows the reflection spectra of black silicon and flat (non-structured) silicon structures for different doping concentrations. Clearly, the reflection from silicon surface is significantly reduced in the case of black silicon compared to the bare silicon. As expressed in equation 2.70 plasma frequency increases with increasing carrier concentration. Therefore, reflection minimum shifts to shorter wavelengths for both black and flat silicon structures with increasing carrier concentration. Around the plasma frequency, since the real part of the permittivity is very low, light can easily penetrate through the material and it is absorbed due to the finite absorption coefficient.

Due to high loss coefficient of highly doped silicon, absorption occurs at the region very close to the surface. Figure 5.3b shows simulated absorption spectra of black and flat silicon structures for different doping concentrations. For practical applications, it is desirable to reduce the electrical thickness of the absorbers as much as possible without compromising its efficiency and bandwidth. Therefore, in these simulations absorption is calculated for 4 μm thick silicon, which is the optimal thickness providing wideband and near perfect absorption. As shown in the figure absorption peak of flat silicon makes a blue shift as doping concentration increases. Similarly, absorption peak of black silicon also makes a blue shift with increasing doping concentration, but in this case absorption efficiency and waveband considerably increased compared to that of flat silicon.

Reflection measurements of fabricated sample was taken with Bruker HYPERION 2000 IR microscope and Bruker Vertex 70v Fourier transform infrared spectrometer. The measurements are referenced to a gold-coated flat silicon mirror. Measured reflection spectrum of black silicon sample is shown in figure 5.4. Using optical constants FDTD simulations and analytical calculations were conducted. Simulated and analytical reflection spectra are also shown in figure 5.4. As shown in the figure, both simulated and analytical reflection spectra have similar trend with measured reflection spectrum.

5.4 Conclusion

In summary, we have demonstrated black silicon absorbers for mid-infrared applications. We fabricated our sample with a Bosch process which is allowing for cost-effective and wafer-scale fabrication. We showed that absorption spectrum can be tuned by controlling the doping concentration of silicon substrates. Fabricated black silicon structures were modeled both numerically and analytically. Both simulation results and analytical results well estimated the experiments. Silicon-based strong absorption of EM wave at mid-infrared region is very promising for realization of opto-electronic devices such as infrared imagers and sensors. Combined with extensive processing and device design knowledge base of silicon, presented absorbers yield fabrication simplicity and provide chip-scale integration compatible with CMOS technology.

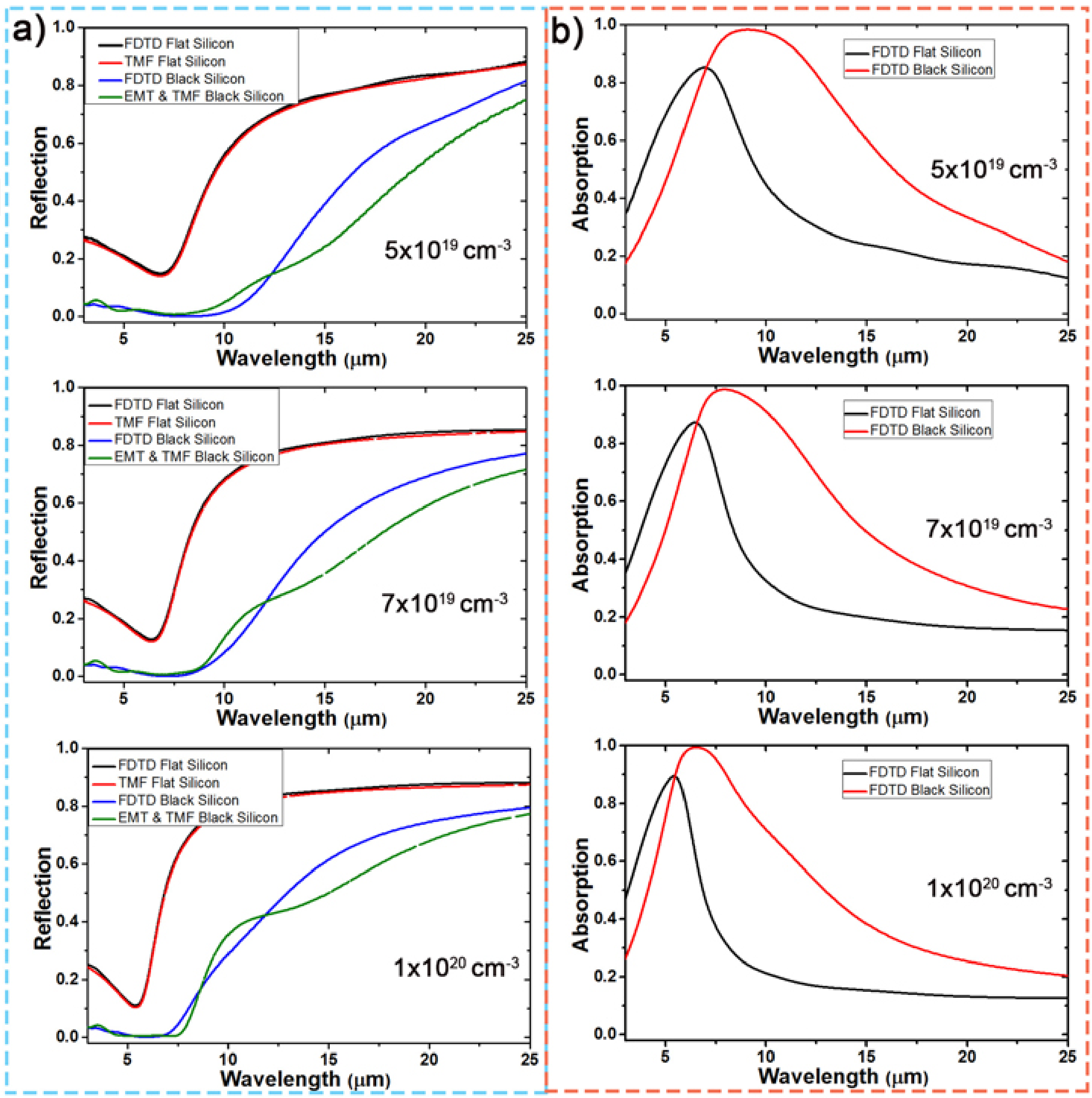

Figure 5.3: (a) Simulated and analytical reflection spectra of flat and black silicon for three different doping concentrations. (b) Simulated absorption spectra of flat silicon and black silicon with thickness of 4 μm for three different doping concentrations.

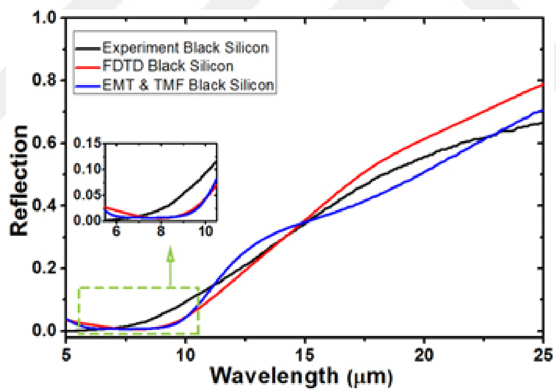

Figure 5.4: Experimental, simulated and analytical reflection spectra for the fabricated sample.

Chapter 6

Conclusions

In this thesis, highly doped silicon is investigated as a promising photonic material for mid-infrared regime. Optical properties of silicon can be changed by tuning its carrier concentration and thus the plasma frequency. Plasma frequency of the silicon is the transition frequency where optical properties of the silicon change from dielectric to metallic response. Plasma frequency of sufficiently doped silicon can come to mid-infrared range. Around plasma frequency it can be possible to design efficient narrowband or broadband absorbers.

We first proposed highly doped silicon based absorbers with a patterned silicon-on-insulator substrate that provide enhanced bandwidth without compromising absorption performance. Broadband absorption is achieved by the combined effects of free carrier absorption, and vibrational and plasmonic absorption resonances. The absorbers, consisting of periodically arranged silicon gratings, is fabricated using standard optical lithography and deep reactive ion etching techniques, allowing for cost-effective and wafer-scale fabrication of micro-structures. Absorption wavebands in excess of 15 micrometers (520m) are demonstrated with more than 90% average absorptivity. The structures also exhibit broadband absorption performance even at large angles of incidence (=50), and independent of polarization.

We also demonstrate plasmonic perfect absorbers based on high conductivity silicon. Standard optical lithography and reactive ion etching techniques are used for the patterning of the samples. We presented computational and experimental results of surface plasmon resonances excited on a silicon surface at normal and oblique incidences. We experimentally demonstrated our absorbers as ultra-low cost, CMOS-compatible and efficient refractive index sensing surfaces. The experimental results reveal that the structure exhibits a sensitivity of around 11 000 nm/RIU and a figure of merit of up to 2.5. We also show that the sensing performance of the structure can be improved by increasing doping density.

Finally, we investigated the absorption of mid-infrared light by low resistivity silicon textured via deep reactive ion etching. An analytical description of the wave propagation in black silicon texture is presented, showing agreement with the experiment and the computational analysis. We also study the dependence of absorption spectrum of black silicon structure on the electrical conductivity of silicon substrate. The structures investigated unveil wideband, all-silicon infrared absorbers applicable for infrared imaging and spectroscopy with simple CMOS compatible fabrication suitable for optoelectronic integration.

Bibliography

[1] M. A. Kats, R. Blanchard, P. Genevet, and F. Capasso, “Nanometre optical coatings based on strong interference effects in highly absorbing media,” *Nature materials*, vol. 12, no. 1, pp. 20–24, 2013.

[2] G. Kajtár, M. Kafesaki, E. Economou, and C. Soukoulis, “Theoretical model of homogeneous metal–insulator–metal perfect multi-band absorbers for the visible spectrum,” *Journal of Physics D: Applied Physics*, vol. 49, no. 5, p. 055104, 2016.

[3] M. Poyraz, K. Gorgulu, Z. Sisman, M. Y. Tanrikulu, and A. K. Okyay, “Lwir all-atomic layer deposition zno bilayer microbolometer for thermal imaging,” *Optical Engineering*, vol. 56, no. 3, pp. 037106–037106, 2017.

[4] C. M. Watts, X. Liu, and W. J. Padilla, “Metamaterial electromagnetic wave absorbers,” *Advanced materials*, vol. 24, no. 23, 2012.

[5] F. Ding, Y. Cui, X. Ge, Y. Jin, and S. He, “Ultra-broadband microwave metamaterial absorber,” *Applied physics letters*, vol. 100, no. 10, p. 103506, 2012.

[6] H. Tao, C. Bingham, D. Pilon, K. Fan, A. Strikwerda, D. Shrekenhamer, W. Padilla, X. Zhang, and R. Averitt, “A dual band terahertz metamaterial absorber,” *Journal of physics D: Applied physics*, vol. 43, no. 22, p. 225102, 2010.

[7] Y. Avitzour, Y. A. Urzhumov, and G. Shvets, “Wide-angle infrared absorber based on a negative-index plasmonic metamaterial,” *Physical Review B*, vol. 79, no. 4, p. 045131, 2009.

[8] S. Ayas, H. Guner, B. Turker, O. O. Ekiz, F. Dirisaglik, A. K. Okyay, and A. Dana, "Raman enhancement on a broadband meta-surface," *ACS nano*, vol. 6, no. 8, pp. 6852–6861, 2012.

[9] A. Tittl, P. Mai, R. Taubert, D. Dregely, N. Liu, and H. Giessen, "Palladium-based plasmonic perfect absorber in the visible wavelength range and its application to hydrogen sensing," *Nano letters*, vol. 11, no. 10, pp. 4366–4369, 2011.

[10] N. Liu, M. Mesch, T. Weiss, M. Hentschel, and H. Giessen, "Infrared perfect absorber and its application as plasmonic sensor," *Nano letters*, vol. 10, no. 7, pp. 2342–2348, 2010.

[11] R. Adato and H. Altug, "In-situ ultra-sensitive infrared absorption spectroscopy of biomolecule interactions in real time with plasmonic nanoantennas," *Nature communications*, vol. 4, 2013.

[12] Y. Shen, J. Zhou, T. Liu, Y. Tao, R. Jiang, M. Liu, G. Xiao, J. Zhu, Z.-K. Zhou, X. Wang, *et al.*, "Plasmonic gold mushroom arrays with refractive index sensing figures of merit approaching the theoretical limit," *Nature communications*, vol. 4, 2013.

[13] Y. Zhong, S. D. Malagari, T. Hamilton, and D. Wasserman, "Review of mid-infrared plasmonic materials," *Journal of Nanophotonics*, vol. 9, no. 1, pp. 093791–093791, 2015.

[14] G. V. Naik, V. M. Shalaev, and A. Boltasseva, "Alternative plasmonic materials: beyond gold and silver," *Advanced Materials*, vol. 25, no. 24, pp. 3264–3294, 2013.

[15] Y. E. Kesim, E. Battal, and A. K. Okyay, "Plasmonic materials based on zno films and their potential for developing broadband middle-infrared absorbers," *AIP Advances*, vol. 4, no. 7, p. 077106, 2014.

[16] L. Baldassarre, E. Sakat, J. Frigerio, A. Samarelli, K. Gallacher, E. Calandrini, G. Isella, D. J. Paul, M. Ortolani, and P. Biagioni, "Midinfrared plasmon-enhanced spectroscopy with germanium antennas on silicon substrates," *Nano letters*, vol. 15, no. 11, pp. 7225–7231, 2015.

[17] M. Shahzad, G. Medhi, R. E. Peale, W. R. Buchwald, J. W. Cleary, R. Soref, G. D. Boreman, and O. Edwards, "Infrared surface plasmons on heavily doped silicon," *Journal of Applied Physics*, vol. 110, no. 12, p. 123105, 2011.

[18] J. C. Ginn, R. L. Jarecki Jr, E. A. Shaner, and P. S. Davids, "Infrared plasmons on heavily-doped silicon," *Journal of Applied Physics*, vol. 110, no. 4, p. 043110, 2011.

[19] J. Cleary, R. Peale, D. Shelton, G. Boreman, C. Smith, M. Ishigami, R. Soref, A. Drehman, and W. Buchwald, "Ir permittivities for silicides and doped silicon," *JOSA B*, vol. 27, no. 4, pp. 730–734, 2010.

[20] E. D. Palik, "Gallium arsenide (gaas)," *Handbook of optical constants of solids*, vol. 1, pp. 429–443, 1985.

[21] T. Xu, Y.-K. Wu, X. Luo, and L. J. Guo, "Plasmonic nanoresonators for high-resolution colour filtering and spectral imaging," *Nature communications*, vol. 1, p. 59, 2010.

[22] D. K. Gramotnev and S. I. Bozhevolnyi, "Plasmonics beyond the diffraction limit," *Nature photonics*, vol. 4, no. 2, pp. 83–91, 2010.

[23] J. A. Dionne, L. A. Sweatlock, M. T. Sheldon, A. P. Alivisatos, and H. A. Atwater, "Silicon-based plasmonics for on-chip photonics," *IEEE Journal of Selected Topics in Quantum Electronics*, vol. 16, no. 1, pp. 295–306, 2010.

[24] S. Law, L. Yu, A. Rosenberg, and D. Wasserman, "All-semiconductor plasmonic nanoantennas for infrared sensing," *Nano letters*, vol. 13, no. 9, pp. 4569–4574, 2013.

[25] S. Law, C. Roberts, T. Kilpatrick, L. Yu, T. Ribaudo, E. Shaner, V. Podolskiy, and D. Wasserman, "All-semiconductor negative-index plasmonic absorbers," *Physical review letters*, vol. 112, no. 1, p. 017401, 2014.

[26] J. Jung and T. G. Pedersen, "Analysis of plasmonic properties of heavily doped semiconductors using full band structure calculations," *Journal of Applied Physics*, vol. 113, no. 11, p. 114904, 2013.

[27] A. Gok, M. Yilmaz, N. Bıyıklı, K. Topallı, and A. K. Okyay, "Practical multi-featured perfect absorber utilizing high conductivity silicon," *Journal of Optics*, vol. 18, no. 3, p. 035002, 2016.

[28] R. J. Walters, R. V. van Loon, I. Brunets, J. Schmitz, and A. Polman, "A silicon-based electrical source of surface plasmon polaritons," *Nature Materials*, vol. 9, no. 1, pp. 21–25, 2010.

[29] R. Soref, "Mid-infrared photonics in silicon and germanium," *Nature photonics*, vol. 4, no. 8, pp. 495–497, 2010.

[30] L.-W. Chou, N. Shin, S. V. Sivaram, and M. A. Filler, "Tunable mid-infrared localized surface plasmon resonances in silicon nanowires," *Journal of the American Chemical Society*, vol. 134, no. 39, pp. 16155–16158, 2012.

[31] W. DiPippo, B. J. Lee, and K. Park, "Design analysis of doped-silicon surface plasmon resonance immunosensors in mid-infrared range," *Optics express*, vol. 18, no. 18, pp. 19396–19406, 2010.

[32] Y.-B. Chen, "Development of mid-infrared surface plasmon resonance-based sensors with highly-doped silicon for biomedical and chemical applications," *Optics express*, vol. 17, no. 5, pp. 3130–3140, 2009.

[33] Y.-B. Chen and Z. Zhang, "Heavily doped silicon complex gratings as wavelength-selective absorbing surfaces," *Journal of Physics D: Applied Physics*, vol. 41, no. 9, p. 095406, 2008.

[34] F. Marquier, K. Joulain, J.-P. Mulet, R. Carminati, and J.-J. Greffet, "Engineering infrared emission properties of silicon in the near field and the far field," *Optics communications*, vol. 237, no. 4, pp. 379–388, 2004.

[35] P. Bouchon, C. Koechlin, F. Pardo, R. Haïdar, and J.-L. Pelouard, "Wideband omnidirectional infrared absorber with a patchwork of plasmonic nanoantennas," *Optics letters*, vol. 37, no. 6, pp. 1038–1040, 2012.

[36] Y. Cui, K. H. Fung, J. Xu, H. Ma, Y. Jin, S. He, and N. X. Fang, "Ultrabroadband light absorption by a sawtooth anisotropic metamaterial slab," *Nano letters*, vol. 12, no. 3, pp. 1443–1447, 2012.

[37] J. Zhou, A. F. Kaplan, L. Chen, and L. J. Guo, "Experiment and theory of the broadband absorption by a tapered hyperbolic metamaterial array," *ACS Photonics*, vol. 1, no. 7, pp. 618–624, 2014.

[38] Z. H. Jiang, S. Yun, F. Toor, D. H. Werner, and T. S. Mayer, "Conformal dual-band near-perfectly absorbing mid-infrared metamaterial coating," *ACS nano*, vol. 5, no. 6, pp. 4641–4647, 2011.

[39] X. Liu, T. Tyler, T. Starr, A. F. Starr, N. M. Jokerst, and W. J. Padilla, "Taming the blackbody with infrared metamaterials as selective thermal emitters," *Physical review letters*, vol. 107, no. 4, p. 045901, 2011.

[40] K. Gorgulu, A. Gok, M. Yilmaz, K. Topalli, N. Bıyıklı, and A. K. Okyay, "All-silicon ultra-broadband infrared light absorbers," *Scientific Reports*, vol. 6, 2016.

[41] R. Kitamura, L. Pilon, and M. Jonasz, "Optical constants of silica glass from extreme ultraviolet to far infrared at near room temperature," *Applied optics*, vol. 46, no. 33, pp. 8118–8133, 2007.

[42] A. Moreau, C. Ciraci, J. J. Mock, R. T. Hill, Q. Wang, B. J. Wiley, A. Chilkoti, and D. R. Smith, "Controlled-reflectance surfaces with film-coupled colloidal nanoantennas," *Nature*, vol. 492, no. 7427, pp. 86–89, 2012.

[43] M. G. Nielsen, A. Pors, O. Albrektsen, and S. I. Bozhevolnyi, "Efficient absorption of visible radiation by gap plasmon resonators," *Optics express*, vol. 20, no. 12, pp. 13311–13319, 2012.

[44] W. Kim, B. S. Simpkins, J. P. Long, B. Zhang, J. Hendrickson, and J. Guo, "Localized and nonlocalized plasmon resonance enhanced light absorption in metal-insulator-metal nanostructures," *JOSA B*, vol. 32, no. 8, pp. 1686–1692, 2015.

[45] R. Nicolas, G. Lévêque, J. Marae-Djouda, G. Montay, Y. Madi, J. Plain, Z. Herro, M. Kazan, P.-M. Adam, and T. Maurer, "Plasmonic mode interferences and fano resonances in metal-insulator-metal nanostructured interface," *Scientific reports*, vol. 5, p. 14419, 2015.

[46] G. Tagliabue, C. Höller, H. Eghlidi, and D. Poulikakos, "Proximal gap-plasmon nanoresonators in the limit of vanishing inter-cavity separation," *Nanoscale*, vol. 6, no. 17, pp. 10274–10280, 2014.

[47] M. G. Nielsen, D. K. Gramotnev, A. Pors, O. Albrektsen, and S. I. Bozhevolnyi, "Continuous layer gap plasmon resonators," *Optics express*, vol. 19, no. 20, pp. 19310–19322, 2011.

[48] R. Alaee, C. Menzel, U. Huebner, E. Pshenay-Severin, S. Bin Hasan, T. Pertsch, C. Rockstuhl, and F. Lederer, "Deep-subwavelength plasmonic nanoresonators exploiting extreme coupling," *Nano letters*, vol. 13, no. 8, pp. 3482–3486, 2013.

[49] R. Gordon, "Light in a subwavelength slit in a metal: Propagation and reflection," *Physical Review B*, vol. 73, no. 15, p. 153405, 2006.

[50] Ş. E. Kocabaş, G. Veronis, D. A. Miller, and S. Fan, "Modal analysis and coupling in metal-insulator-metal waveguides," *Physical Review B*, vol. 79, no. 3, p. 035120, 2009.

[51] S. A. Maier, *Plasmonics: fundamentals and applications*. Springer Science & Business Media, 2007.

[52] N. I. Landy, S. Sajuyigbe, J. Mock, D. Smith, and W. Padilla, "Perfect metamaterial absorber," *Physical review letters*, vol. 100, no. 20, p. 207402, 2008.

[53] B. Wang, T. Koschny, and C. M. Soukoulis, "Wide-angle and polarization-independent chiral metamaterial absorber," *Physical Review B*, vol. 80, no. 3, p. 033108, 2009.

[54] H. Tao, C. Bingham, A. Strikwerda, D. Pilon, D. Shrekenhamer, N. Landy, K. Fan, X. Zhang, W. Padilla, and R. Averitt, "Highly flexible wide angle of incidence terahertz metamaterial absorber: Design, fabrication, and characterization," *physical review B*, vol. 78, no. 24, p. 241103, 2008.

[55] M. K. Hedayati, M. Javaherirahim, B. Mozooni, R. Abdelaziz, A. Tavassolizadeh, V. S. K. Chakravadhanula, V. Zaporojtchenko, T. Strunkus,

F. Faupel, and M. Elbahri, "Design of a perfect black absorber at visible frequencies using plasmonic metamaterials," *Advanced Materials*, vol. 23, no. 45, pp. 5410–5414, 2011.

[56] T. V. Teperik, F. G. De Abajo, A. Borisov, M. Abdelsalam, P. Bartlett, Y. Sugawara, and J. Baumberg, "Omnidirectional absorption in nanostructured metal surfaces," *Nature photonics*, vol. 2, no. 5, pp. 299–301, 2008.

[57] Y. Yao, R. Shankar, M. A. Kats, Y. Song, J. Kong, M. Loncar, and F. Capasso, "Electrically tunable metasurface perfect absorbers for ultrathin mid-infrared optical modulators," *Nano letters*, vol. 14, no. 11, pp. 6526–6532, 2014.

[58] K. Aydin, V. E. Ferry, R. M. Briggs, and H. A. Atwater, "Broadband polarization-independent resonant light absorption using ultrathin plasmonic super absorbers," *Nature communications*, vol. 2, p. 517, 2011.

[59] S. Law, D. Adams, A. Taylor, and D. Wasserman, "Mid-infrared designer metals," *Optics express*, vol. 20, no. 11, pp. 12155–12165, 2012.

[60] T. Ribaudo, D. W. Peters, A. R. Ellis, P. S. Davids, and E. A. Shaner, "Highly directional thermal emission from two-dimensional silicon structures," *Optics express*, vol. 21, no. 6, pp. 6837–6844, 2013.

[61] K. Gorgulu, A. Gok, M. Yilmaz, K. Topalli, and A. Okyay, "High-conductivity silicon based spectrally selective plasmonic surfaces for sensing in the infrared region," *Journal of Optics*, vol. 19, no. 2, p. 025002, 2016.

[62] M. Iglesias, B. Orge, and J. Tojo, "Refractive indices, densities and excess properties on mixing of the systems acetone+ methanol+ water and acetone+ methanol+ 1-butanol at 298.15 k," *Fluid Phase Equilibria*, vol. 126, no. 2, pp. 203–223, 1996.

[63] F. Cheng, X. Yang, and J. Gao, "Enhancing intensity and refractive index sensing capability with infrared plasmonic perfect absorbers," *Optics letters*, vol. 39, no. 11, pp. 3185–3188, 2014.

[64] I. M. Pryce, Y. A. Kelaita, K. Aydin, and H. A. Atwater, "Compliant metamaterials for resonantly enhanced infrared absorption spectroscopy and refractive index sensing," *ACS nano*, vol. 5, no. 10, pp. 8167–8174, 2011.

[65] A. E. Cetin, D. Etezadi, B. C. Galarreta, M. P. Busson, Y. Eksioglu, and H. Altug, "Plasmonic nanohole arrays on a robust hybrid substrate for highly sensitive label-free biosensing," *ACS Photonics*, vol. 2, no. 8, pp. 1167–1174, 2015.

[66] S. Basu, B. Lee, and Z. Zhang, "Infrared radiative properties of heavily doped silicon at room temperature," *Journal of Heat Transfer*, vol. 132, no. 2, p. 023301, 2010.

[67] R. Singh, A. K. Azad, J. F. O'Hara, A. J. Taylor, and W. Zhang, "Effect of metal permittivity on resonant properties of terahertz metamaterials," *Optics letters*, vol. 33, no. 13, pp. 1506–1508, 2008.

[68] Y. Gu, Q. Li, J. Xiao, K. Wu, and G. P. Wang, "Plasmonic metamaterials for ultrasensitive refractive index sensing at near infrared," *Journal of Applied Physics*, vol. 109, no. 2, p. 023104, 2011.

[69] P. Mandal, "H-shape plasmonic metasurface as refractive index sensor," *Plasmonics*, vol. 10, no. 2, pp. 439–445, 2015.

[70] S. A. Dereshgi and A. K. Okyay, "Large area compatible broadband superabsorber surfaces in the vis-nir spectrum utilizing metal-insulator-metal stack and plasmonic nanoparticles," *Optics Express*, vol. 24, no. 16, pp. 17644–17653, 2016.

[71] M. A. Nazirzadeh, F. B. Atar, B. B. Turgut, and A. K. Okyay, "Random sized plasmonic nanoantennas on silicon for low-cost broad-band near-infrared photodetection," *Scientific reports*, vol. 4, p. 7103, 2014.

[72] F. B. Atar, E. Battal, L. E. Aygun, B. Daglar, M. Bayindir, and A. K. Okyay, "Plasmonically enhanced hot electron based photovoltaic device," *Optics express*, vol. 21, no. 6, pp. 7196–7201, 2013.

[73] C. Shi, X. Zang, Y. Wang, L. Chen, B. Cai, and Y. Zhu, “A polarization-independent broadband terahertz absorber,” *Applied Physics Letters*, vol. 105, no. 3, p. 031104, 2014.

[74] S. Yin, J. Zhu, W. Xu, W. Jiang, J. Yuan, G. Yin, L. Xie, Y. Ying, and Y. Ma, “High-performance terahertz wave absorbers made of silicon-based metamaterials,” *Applied Physics Letters*, vol. 107, no. 7, p. 073903, 2015.

[75] Y. E. Kesim, E. Battal, M. Y. Tanrikulu, and A. K. Okyay, “An all-zno microbolometer for infrared imaging,” *Infrared Physics & Technology*, vol. 67, pp. 245–249, 2014.

[76] E. Battal, S. Bolat, M. Y. Tanrikulu, A. K. Okyay, and T. Akin, “Atomic-layer-deposited zinc oxide as tunable uncooled infrared microbolometer material,” *physica status solidi (a)*, vol. 211, no. 11, pp. 2475–2482, 2014.

[77] M. Steglich, D. Lehr, S. Ratzsch, T. Käsebier, F. Schrempel, E.-B. Kley, and A. Tünnermann, “An ultra-black silicon absorber,” *Laser & Photonics Reviews*, vol. 8, no. 2, pp. L13–L17, 2014.

[78] M. Steglich, T. Käsebier, M. Zilk, T. Pertsch, E.-B. Kley, and A. Tünnermann, “The structural and optical properties of black silicon by inductively coupled plasma reactive ion etching,” *Journal of Applied Physics*, vol. 116, no. 17, p. 173503, 2014.

[79] X. Liu, P. R. Coxon, M. Peters, B. Hoex, J. M. Cole, and D. J. Fray, “Black silicon: fabrication methods, properties and solar energy applications,” *Energy & Environmental Science*, vol. 7, no. 10, pp. 3223–3263, 2014.

[80] M. Otto, M. Algasinger, H. Branz, B. Gesemann, T. Gimpel, K. Füchsel, T. Käsebier, S. Kontermann, S. Koynov, X. Li, *et al.*, “Black silicon photovoltaics,” *Advanced optical materials*, vol. 3, no. 2, pp. 147–164, 2015.

[81] Y.-L. Deng and Y.-J. Juang, “Black silicon sers substrate: effect of surface morphology on sers detection and application of single algal cell analysis,” *Biosensors and Bioelectronics*, vol. 53, pp. 37–42, 2014.

[82] G. Gervinskas, G. Seniutinas, J. S. Hartley, S. Kandasamy, P. R. Stoddart, N. F. Fahim, and S. Juodkazis, "Surface-enhanced raman scattering sensing on black silicon," *Annalen der Physik*, vol. 525, no. 12, pp. 907–914, 2013.

[83] K. Gorgulu, M. Yilmaz, K. Topalli, and A. K. Okyay, "Wideband black siliconfor mid-infrared applications," *Journal of Optics*, 2017.

[84] A. V. Tikhonravov, M. K. Trubetskov, T. V. Amotchkina, and J. Dobrowolski, "Estimation of the average residual reflectance of broadband antireflection coatings," *Applied optics*, vol. 47, no. 13, pp. C124–C130, 2008.

[85] A. Tikhonravov, V. Zhupanov, V. Fedoseev, and M. K. Trubetskov, "Design and production of antireflection coating for the 8–10 μm spectral region," *Optics express*, vol. 22, no. 26, pp. 32174–32179, 2014.

[86] R. R. Willey, *Practical design and production of optical thin films.* CRC Press, 2002.

[87] D. H. Raguin and G. M. Morris, "Antireflection structured surfaces for the infrared spectral region," *Applied Optics*, vol. 32, no. 7, pp. 1154–1167, 1993.

[88] C. A. Foss Jr, M. J. Tierney, and C. R. Martin, "Template synthesis of infrared-transparent metal microcylinders: comparison of optical properties with the predictions of effective medium theory," *The Journal of Physical Chemistry*, vol. 96, no. 22, pp. 9001–9007, 1992.

[89] H. Wang, X. Liu, L. Wang, and Z. Zhang, "Anisotropic optical properties of silicon nanowire arrays based on the effective medium approximation," *International Journal of Thermal Sciences*, vol. 65, pp. 62–69, 2013.

[90] D. Li and C.-Z. Ning, "All-semiconductor active plasmonic system in mid-infrared wavelengths," *Optics express*, vol. 19, no. 15, pp. 14594–14603, 2011.

[91] X. Liu, L. Wang, and Z. Zhang, "Wideband tunable omnidirectional infrared absorbers based on doped-silicon nanowire arrays," *Journal of Heat Transfer*, vol. 135, no. 6, p. 061602, 2013.